# INVESTIGATION OF THERMO-PHYSICAL PROPERTY ENHANCEMENT MECHANISM OF MOLTEN SALT NANO-EUTECTIC VIA NANOSTRUCTURAL CHANGE AND POLYALPHAOLEFIN NANOFLUID VIA IN SITU FORMATION OF SUPERSTRUCTURES

by

ZAHRA POURNOROUZ

Presented to the Faculty of the Graduate School of

The University of Texas at Arlington in Partial Fulfillment

of the Requirements

for the Degree of

DOCTOR OF PHILOSOPHY

THE UNIVERSITY OF TEXAS AT ARLINGTON

August 2018

Acknowledgments

I never took a break from school; I went straight from elementary to middle to high school to college to graduate school, and still can remember my very first day at school, nineteen years ago, full of passion and excitement. Finally, today, more passionate than ever, I get to write the last words of my academic life, and I am pleased to end it by expressing my deepest gratitude to my family.

I would like to dedicate my dissertation to my parents, for trusting me with every single decision I made and being the most supportive people in every moment of my life. I cannot put into words, how privileged, thankful, and proud I am, to have them as my parents.

I would also like to dedicate this dissertation to the love of my life, my husband, Ali, for all his love, support and continuously encouraging me to pursue my dreams.

This dissertation represents the result of many experiences I have encountered at UTA from remarkable individuals who I also wish to acknowledge.

I wish to thank my Ph.D. advisor, Dr. Donghyun Shin, for his guidance, insight, and support throughout this research project.

Besides my advisor, I would like to thank the rest of my dissertation committee: Prof. Dereje Agonafer, Dr. Hyejin Moon, Dr. Ratan Kumar and Dr. Miguel Amaya, for their encouragement, insightful comments, and hard questions.

July 25, 2018

Abstract

INVESTIGATION OF THERMO-PHYSICAL PROPERTY ENHANCEMENT MECHANISM OF MOLTEN SALT NANO-EUTECTIC VIA NANOSTRUCTURAL CHANGE AND POLYALPHAOLEFIN NANOFLUID VIA IN SITU FORMATION OF SUPERSTRUCTURES

Zahra Pournorouz, PhD

The University of Texas at Arlington, 2018

Supervising Professor: Donghyun Shin

For many years, scientists enhanced the specific heat capacity of molten salt nanofluids by dispersing only minute concentrations of different nanoparticles (e.g., 1 wt. %). While the specific heat capacity for molten salts was enhanced in many types of research, other engineering fluids (i.e., water, ethylene glycol, oil) showed decreased specific heat capacity with doping the nanoparticles. Recently, researchers discovered that a unique nanostructure formed by molten salt molecules, which were doped and interacted with nanoparticles, were the reason for enhanced specific heat capacity. Therefore, the enhanced specific heat capacity only happens for molten salts rather than other fluids that may not naturally form these nanostructures. In the first study, the specific heat capacity of molten salt nano-eutectic ($Li_2CO_3 - K_2CO_3$ doped with $SiO_2$ nanoparticles) was theoretically investigated. Corresponding to the proposed theory in the literature [1], the specific heat capacity of a nano-eutectic can be significantly increased by the formation of needle-like nanostructures by salt eutectic. To investigate the effect of the formed nanostructure, the model presented by Wang [2] for nano-sized particles was used and expanded to theoretically calculate the specific heat capacity of the nanostructure of molten salt nano-eutectic. The mass fraction of the formed nanostructure was estimated by MATLAB using the reported material characterization study [3]. The theoretical predictions

were in a good agreement with the measured specific heat capacity values from the literature, with the error of 3 - 4%. An additional verification of the proposed model was done by a different lab partner using a molecular dynamics study. The error between the theoretical prediction and the simulation is only 3.4%, and the value was in a good agreement with the experiment (1.9% max. error) [66]. The result confirms the enhanced specific heat capacity of a nano-eutectic can be described by the contribution of the formed nanostructure. Hence, we artificially fabricated similar nanostructures and dispersed them in a non-salt medium to see whether it enhances specific heat capacity or not. In the second study, we theorized such nanostructures could be mimicked through the *in-situ* formation of fabricated nano-additives, which are the acknowledged nanoparticles coated by organic materials (e.g., polar-group-ended organic molecules) resulting to these structures called superstructures. We first portrayed this approach by studying the polyalphaolefin (PAO) oil as the base fluid and coated the $SiO_2$ nanoparticles with Polyethylene-block-poly (ethylene glycol) (PBP). A differential scanning calorimeter (DSC) device, a discovery hybrid rheometer (HR-2), and an in-lab built thermal conductivity apparatus were used to conduct measurements for the specific heat capacity, thermal conductivity, and viscosity of pure PAO and PAO with fabricated nano-additives. Results showed 44.5% enhancement for specific heat capacity and 19.8% and 22.98% enhancement for thermal conductivity and viscosity, respectively, by adding fabricated superstructures compared to pure PAO. Furthermore, a peak representing the partial melting of the PBP was detected in the first thermal cycle, which disappeared in the following cycles; so, this specifies that the *in-situ* formation of fabricated nano-additives spontaneously happens in the thermal cycle to form such superstructures. At last, we analyzed the figure of merit for PAO-superstructure to evaluate the value of its performance for heat transfer and storage media.

Table of Contents

List of Illustrations

List of Tables

# Chapter 1

# Introduction

## *1.1. Nanofluid*

A nanoparticle suspended in a liquid forms the nanofluid, which was first presented in 1995 by Choi et al. [4]. Nanofluids cause more resourceful energy generation and usage which decreases the amount of maintenance, repair, construction and withdraw activities in the military and they also have many applications in heat transfer, automotive, electronic, and biomedical industries.

The heat transfer applications [5] include the following: 1) mechanical cooling, which would result in tremendous energy savings; 2) smart fluid, in which the nanofluid would work as a heat valve for controlling the heat flow; 3) nuclear reactors, nanofluid will improve the critical heat flux of the coolant, resulting in an economic profit while increasing the safety standard related to the power plant system; 4) withdrawal of geothermal power, in which the role of the nanofluids is to cool down the pipes operated in very high temperature and high friction.

The automotive applications [5] include the following: 1) coolant, in which using a nanofluid would result in shrinking the size and better locating of radiators, the nanofluid will result in higher efficiency so that the coolant pump can shrink; 2) fuel, nanofluids in the combustion of diesel increases the total combustion heat and decreases the concentration of the nitrous and smoke in the exhaust emissions; 3) brake, nanofluids will enhance the characteristics of the braking oil resulting in increased performance in heat transfer.

The electronic applications [5] include the following: 1) cooling in microchips, since the thermal conductivity in microchips is so high, the nanofluid would be an excellent choice as a cooling liquid; 2) fluidic applications in microscale, nanofluids can

be used to engineer the wettability of the surface and the surface tension in MEMs applications.

The biomedical applications [5] include the following: 1) nano drug delivery, in which nanofluid will help drug-concentration uniformity; 2) cancer Therapeutics, for example, the magnetic nanofluids are a way to help and guide the particles to go up through the bloodstream to a tumor, therefore the doctors would be able to deliver the high dose of drugs to the tumor without hurting any healthy tissues; 3) cryopreservation; 4) nanocryosurgery; 5) sensing and imaging.

Knowing all the applications for nanofluid, the reason that nanofluid benefits these previously mentioned applications was investigated. Nanofluids tend to increase the thermo-physical properties of the base fluid, such as specific heat capacity, thermal conductivity, and viscosity.

### *1.2. The thermal conductivity of nanofluid*

Nanofluids have been studied by many researchers, scientists, and engineers for their enhancement effect on thermal conductivity [4], [6]–[11]. Metal nanoparticles, oxide nanoparticles, and carbon-based nanoparticles (i.e., carbon nanotube or graphene) dispersed in common engineering fluids (i.e., water, ethylene glycol or any oil) have shown significantly enhanced thermal conductivity.

Several researchers have represented theories to explain the increase in the thermal conductivity measurements, including: 1) “the Brownian motion of nanoparticles,” which is a random motion of the suspended particles in the base fluid and transfers energy directly by nanoparticle, and it is a micro-convection effect due to the mixture of the fluid with nanoparticles; 2) “the liquid molecule layered around the nanoparticles,” that is the layered structures of liquid molecules around solid surfaces, and the nanolayers have higher effective thermal conductivity than the liquid matrix; 3) “The heat transfer of

the nanoparticles;" 4) "percolation grid by aggregated nanoparticles" [12]–[18] . However, none could clearly explain the underlying mechanism behind nanofluid. Later, it was commonly agreed that a modified useful medium theory with aggregated nanoparticle network could estimate the observed enhanced thermal conductivity [18], [19].

Table 1-1 A summary of literature review for enhanced thermal conductivity in nanofluid

| 1st Author | Nanoparticle / Base fluid | Concentration (vol. %) | Enhancement (%) |
|---|---|---|---|
| Lee [20] | $Al_2CO_3$ / Water | 4.0 | 23 |
| Xie [21] | SiC / Water | 4.18 | 17 |
| Hong [22] | Fe / Ethylene glycol | 0.55 | 18 |
| Assael [23] | CNT / Water | 0.6 | 38 |
| Das [10] | CuO / Water | 4.0 | 36 |
| Eastman [8] | Cu / Ethylene glycol | 3.6 | 10 |

### *1.3. The viscosity of nanofluid*

Nanoparticle addition in a fluid increases the viscosity of the base fluid. Researchers did several experiments to show variation of the nanoparticle effect on base fluid and proved that the increase in viscosity has not much effect on thermal performance of the base fluid, because the thermal conductivity enhancement is much higher than the increase in viscosity and prevents the thermal performance of going down. For example, Prasher et al. [24] experimentally investigated the viscosity of alumina-based nanofluid and got 23% enhancement, and confirmed that the increase in the viscosity of their nanofluid should be 4 times larger to have an effect on thermal conductivity.

Table 1-2 A summary of literature review for enhanced thermal conductivity in nanofluid

| 1st Author | Nanoparticle / Base fluid | Concentration (%) | Enhancement (%) |
|---|---|---|---|
| Perashel [24] | $Al_2CO_3$ / PG | 4.0 | 23 |
| Chen [25] | $TiO_2$ / Ethylene Glycol | 0.25 - 1.2 | 3 - 11 |
| Chandresakar [26] | $Al_2CO_3$ / Water | 1 - 5 | 14 - 136 |
| Nguyen [27] | $Al_2CO_3$ / Water | 2.1 - 13 | 10 - 210 |
| He [28] | $TiO_2$ / DW | 0.024 - 1.18 | 4 - 11 |

### *1.4. The specific heat capacity of nanofluid*

While there are some studies for the enhancement of the effective thermal conductivity in nanofluids, divisive results have been published for the specific heat capacity of the nanofluids. The specific heat capacity of the conventional water and organic solvent-based nanofluids decreased while doped with nanoparticles [29]–[31]. For example, $SiO_2$ nanoparticle suspension with 10 vol. % concentration in water had -12% effect on the specific heat capacity of water [29]. Alumina nanoparticle dispersion with 21.7 vol. % decreased the specific heat capacity of the water by 40% [30]. Specific heat capacity of the mixture of water and ethylene glycol showed a 20% decrease with only 7 vol. % addition of $ZnO$ nanoparticles [31]. Such negative effects of the specific heat capacity is because most solid nanoparticles have lower specific heat capacity than the known base fluids such as water, ethylene glycol or oil, and the observed decrease were in a good agreement with the conventional specific heat capacity formula based on a density weighted mixing law as follows [32]:

$$C_{p,nf} = \frac{m_{np}C_{p,np} + m_{bf}C_{p,bf}}{m_{np} + m_{bf}} \quad (1)$$

Where $C_{p,nf}$, $C_{p,np}$ and $C_{p,bf}$ are the specific heat capacity of nanofluid, nanoparticle, and base fluid, respectively. $m_{np}$ and $m_{bf}$ are the mass of the nanoparticle and the base fluid, respectively.

*1.4.1. Molten salt nanofluid*

Although water-based nanofluids regularly had an adverse effect on the specific heat capacity of the base fluid by addition of nanoparticles, the specific heat capacity of the molten salt eutectic was enhanced with the addition of nanoparticles [1], [3], [33]–[44]. Subsequently, as was first introduced in 2011 [33], [34], various eutectics of molten salts were doped with nanoparticles to enhance their specific heat capacity values. $Li_2CO_3 - K_2CO_3$ doped with $SiO_2$ nanoparticles, $Al_2O_3$ nanoparticles, $MgO$ nanoparticles, or multi-walled carbon nanotubes have shown around 20~120% specific heat capacity enhancement with only 1% concentration [33], [40], [45]–[47]. $Li_2CO_3 - Na_2CO_3 - K_2CO_3$ doped with $Al_2O_3$ nanoparticles at 1% concentration was reported for 33% enhanced specific heat capacity [48]. $NaNO_3 - KNO_3$ doped with various nanoparticles have shown enhanced specific heat capacity at a wide range of nanoparticle concentrations [1], [36], [38], [43], [44], [49]–[52]. $LiNO_3 - NaNO_3 - KNO_3$ was mixed with $SiO_2$ nanoparticles at different sizes, and its specific heat capacity was enhanced up to 16% [39], [42]. $NaNO_3 - KNO_3 - \mathrm{Ca}(NO_3)_2$ was doped with $SiO_2$ nanoparticles and its specific heat capacity was enhanced by 19% [53]. $KNO_3 - NaNO_2 - NaNO_3$ has shown enhanced specific heat capacity of 20% at a very small concentration (0.06 wt. %) [35], [54]. $\mathrm{Ca}(NO_3)_2 - NaNO_3 - KNO_3 - LiNO_3$ was tested with $SiO_2$ nanoparticles and showed 20% specific heat capacity enhancement at 1% concentration [55]. $C_{12}H_{10} - C_{12}H_{10}O$ doped with $Cu$ nanoparticles only at 0.01 wt.% concentration was reported for 15%

enhanced specific heat capacity [56]. $NaCl - CaCl_2$ doped with expanded graphite has shown an increase of specific heat capacity with temperature [57]. $BaCl_2 - CaCl_2 - NaCl - LiCl$ doped with $SiO_2$ nanoparticles (1 wt.% concentration) was reported for its enhanced specific heat capacity by 15% [34]. While various nano-eutectics were reported for their enhanced specific heat capacity measured experimentally, there was almost no study reported to theoretically estimate the enhanced specific heat capacity by nano-eutectics.

Table 1-3 A summary of literature review for specific heat capacity enhancement

| | 1st Author | Nanoparticle / Base fluid | Concentration (%) | Enhancement (%) |
|---|---|---|---|---|
| Conventional nanofluid | Zhou [30] | $Al_2CO_3$ / Water | 21.7 vol. | - 40 |
| | Namburu [29] | $SiO_2$ / Water | 10 vol. | -12 |
| | Vajjha [31] | ZnO / Ethylene glycol & Water | 7 vol. | -20 |
| Salt nanofluid | Shin [33] | $SiO_2$ / $Li_2CO_3 - K_2CO_3$ | 1.0 wt. | 19 |
| | Xi Ho [35] | $Al_2CO_3$ / $NaNO_3$-$KNO_3$-$NaNO_2$ | 0.063 wt. | 19.9 |
| | Chierruzzi [49] | $SiO_2$ / $NaNO_3$-$KNO_3$ | 1.0 wt. | 15 |
| | Andreu-Cabedo [44] | $SiO_2$ / $NaNO_3$-$KNO_3$ | 1.0 wt. | 25.03 |
| | Schuller [36] | $Al_2CO_3$ / $NaNO_3$-$KNO_3$ | 2.0 wt. | 30.6 |

Table 1.3—*Continued*

| | | | | |
|---|---|---|---|---|
| | Lasfargues [1] | $TiO_2$ / $NaNO_3$-$KNO_3$ | 3.0 wt. | 7.5 |
| | Qiao [37] | $SiO_2$ / $LiNO_3$-$NaNO_3$-$KNO_3$ | 6.0 wt. | 20 |
| | Tiznobaik [3] | $SiO_2$ / $Li_2CO_3 - K_2CO_3$ | 1.0 wt. | 25 |
| | Dudda [38] | $SiO_2$ / $NaNO_3$-$KNO_3$ | 1.0 wt. | 27 |

The nanoparticles implanted for the molten salts characteristically have lower specific heat capacity compared to the base material, which is molten salts, and the current density weighted model (Equation 1) was not able to explain the enhancement of the experimentally measured specific heat capacity. The failure of equation 1 indicates that a different heat storage mechanism may be in the mixture other than nanoparticles and molten salts, which is the reason for the enhanced specific heat capacity. Based on principles in recent studies [45], [58], molten salt molecules are likely to form a fractal-like shaped nanostructure by dispersing the nanoparticles. However, the formation of these nanostructures is indistinct. Up to now, two reasons were presented that might be the reason for the formation of the nanostructures; 1) unique feature of salt eutectic (i.e., the mixture of two or more salts in order to decrease its melting point); 2) electrostatic interface of salt molecule to a nanoparticle (which has a different interaction with each kind of salt) [45], [58].

Hence, a few efforts were made by molten salt nanofluid researchers to describe the enhanced specific heat capacity of nano-eutectics include the following: 1) enhanced specific heat capacity of the nanoparticles; 2) the interfacial thermal resistance; and 3) semi-solid layering by liquid salts near nanoparticles [33], [49], [59]. Recent studies have

shown that molten salt eutectics are expected to shape a semi-solid nanostructure on a nanoparticle surface [40], [45].

Dispersing the nanoparticles into a eutectic molten salt mixture causes the nanoparticle charged negatively on the surface. The eutectic composition ratio of the salt mixture changes and causes each salt element to interact differently with the nanoparticle within its electric double layer (EDL) (Figure 1-1). As shown in the phase diagram (Figure 1-2), within the EDL of a nanoparticle, one salt (salt A) moves close to the nanoparticle, while the other salt (salt B) goes far from the nanoparticle. Hence, the mixing ratio moves toward salt A within the EDL (red arrow). Salt A then needs to solidify to return to the eutectic point for the salt mixture to remain in the liquid phase. The nanoparticle presents itself as a nucleating site for Salt A to grow to shape a nanostructure resembling dendrites (Figure 1-3). The mixture ratio of the eutectic salt is a very important factor to control the enhancement of the specific heat capacity, for example increasing the ratio of salt A in the eutectic mixture (Figure 1-2) means moving towards the left side of the phase diagram, and since the salt A is the one that crystallized on the nanoparticle surface, we would have more fractal-like nanostructures, resulting to even more surface to volume ratio for the nanostructures, therefore the higher the ratio of salt A in the eutectic mixture, the more is the enhancement of the specific heat capacity of the nanofluid. This theory confirmed by a backscattered electron micrograph [3], that a formed nanostructure has a different molar composition from its eutectic point, indicating nanostructures consist of the excess salt beyond its eutectic point (i.e., salt A (solid) in Figure 1-2).

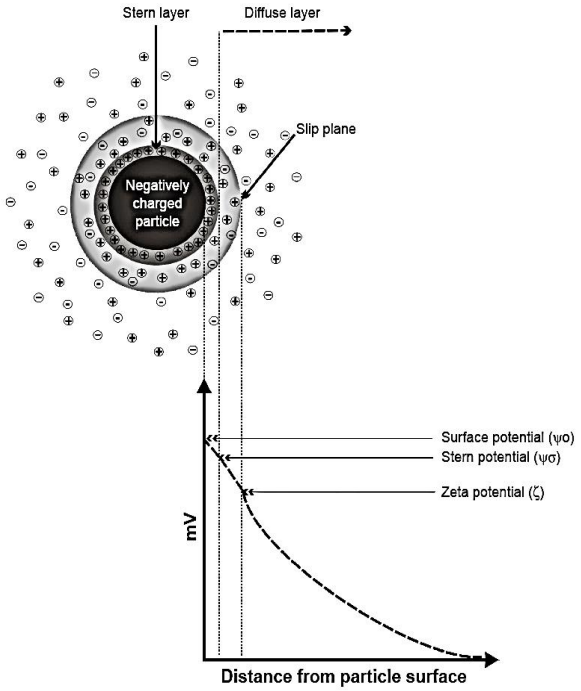


Figure 1-1 Schematic of the electric double layer of a nanoparticle suspended in a base fluid, and the graphical response produced by the analysis [60]

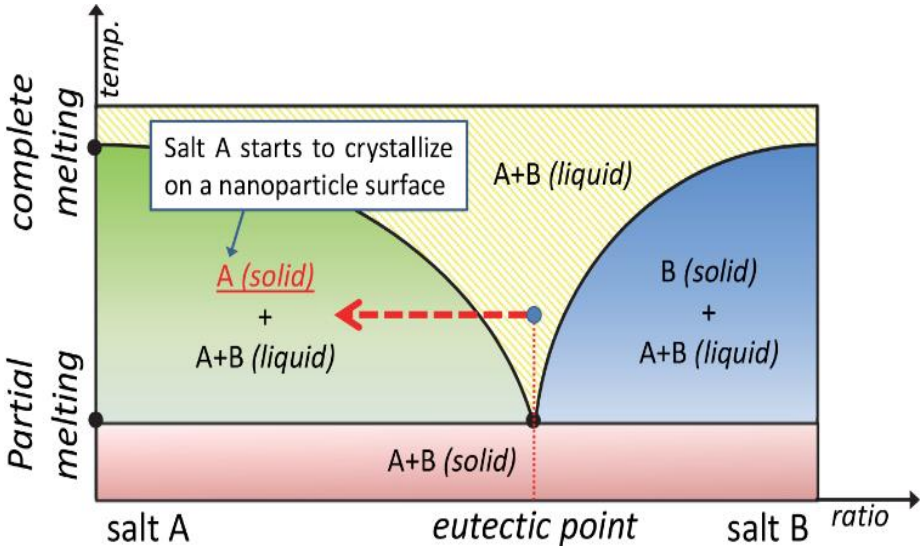


Figure 1-2 A phase diagram of a eutectic of molten salts (i.e., a mixture of two salts (A+B)) [61]

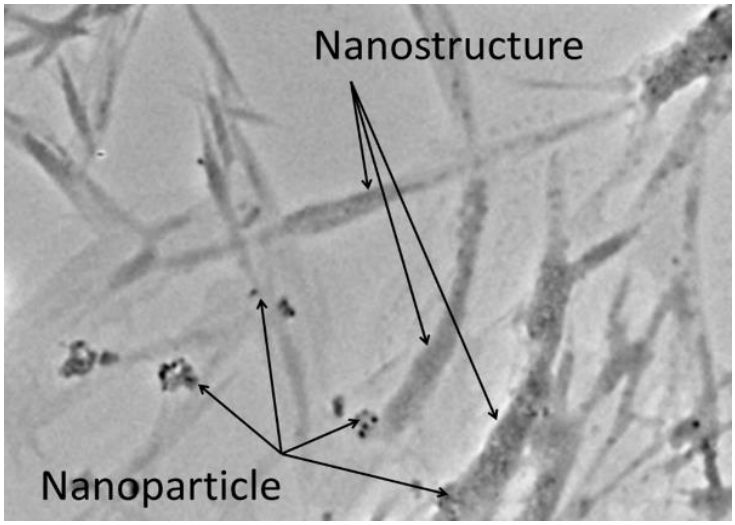


Figure 1-3 A TEM image of dendritic nanostructure formed by salt eutectic near nanoparticles ($Li_2CO_3 - K_2CO_3$ eutectic doped with $SiO_2$ nanoparticles) [58].

The electrostatic effect may not only dominate the separation and growth phenomena. Since the electrostatic force differs between each salt to a nanoparticle, this results in the crystallization of the separated salt molecules on the nanoparticle surface. The nanoparticle surface presents itself as a nucleation point and grows to shape a fractal-like nanostructure [45], [58]. There are some other mechanisms presented by some researchers which are 1) the polarization of molten salt ions [62], 2) the multicomponent diffusional mechanisms of molten salts [63], or a 3) combined effect of number 1 and 2.

Since the fractal-like nanostructures have an extensive interfacial surface area to their volume, this explained the reason for the enhanced specific heat capacity. Many researchers have experimentally and analytically proven the effect of enormously enlarged surface areas on the effective specific heat capacity [2], [64] [65]. Qiao et al.

[37] efficaciously conducted molecular dynamics simulations to foresee such an enhanced specific heat capacity of trinary nitrate salt ($LiNO_3 - NaNO_3 - KNO_3$) when dispersed with $SiO_2$ nanoparticles.

Although the growth of these salts from a few nanometers to a tens of nanometers level is not fully discovered, many researchers have shown the effectiveness of the fractal-like nanostructures on the specific heat capacity. Since these nanostructures have extensive specific surface areas, they can expressively increase the effect of surface energy on the overall specific heat capacity (although this effect is generally negligible in macroscopic heat transfer). Wang et al. [64] experimentally proved the enhancement of specific heat capacity of nanostructured $Al_2O_3$ by 25% in comparison to bulk $Al_2O_3$ . Wang et al. [2] theoretically proved that increasing a specific surface area at a nanoscale enhances the effective specific heat capacity of copper nanoparticles. A similar approach was also applied to other nanostructured materials, such as silver and titanium oxide[65]–[67]. However, these studies are simple one-to-one comparisons between nanoparticles and their bulks and, therefore, cannot be applied to the reported molten salt-based nano-eutectics directly.

Hence, in the first study, we used the available theoretical model from a literature along with the reported thermal and material characterization results to see whether we can predict the experimentally measured enhancement in specific heat capacity. We also repeated the theory for different sizes and concentrations of the same materials to better verify the results. To the best of our knowledge, this is the very first attempt to approximate the enhanced specific heat capacity of a nano-eutectic quantitatively.

*1.4.2. Conventional nanofluid*

The fractal-like nanostructures formed only by molten salt molecules have not naturally formed in other non-salt fluids. Therefore, such a phenomenon may be the

reason for the decreased specific heat capacity of water, oil, and ethylene glycol-based nanofluids with dispersed nanoparticles [29]–[31]. Thus, it is essential to discover the applicability of the fractal-like nanostructure into these common engineering fluids. As a result of the first study and explaining the concept of nanostructures, we moved on to conventional nanofluids and researched how to enhance the specific heat capacity of those nanofluids and find the reason that nobody ever could do that.

Consequently, in the second study, we theorized such nanostructures could be mimicked through the in-situ formation of fabricated nano-additives doped with nanoparticles, coated with polar-group-ended organic molecules (called superstructure), so it can be dispersed simply into other engineering fluids.

We first conducted the experiments for this methodology using polyalphaolefin (PAO). Hydroxy-ended poly (ethylene glycol) [MW ca. 1,400] (PBP) and $SiO_2$ nanoparticles and were selected to be dispersed into the PAO to artificially form a nanostructure on the nanoparticle surface. Precisely, we predicted that dispersing the fabricated nano-additives along with the nanoparticles together into PAO can originate in-situ formation of the superstructure, resulting in the enhanced specific heat capacity of PAO together with other thermophysical properties, such as viscosity and thermal conductivity. Accordingly, a figure of merit analysis has been done for PAO-nanostructure to estimate its performance for heat transfer and heat storage media.

Figure 1-4 shows the nanostructures formed in the molten salt. We used the same idea to apply to our theoretical model in the first study, and figure 1-5 presents a schematic of the proposed synthesis used in the second study.

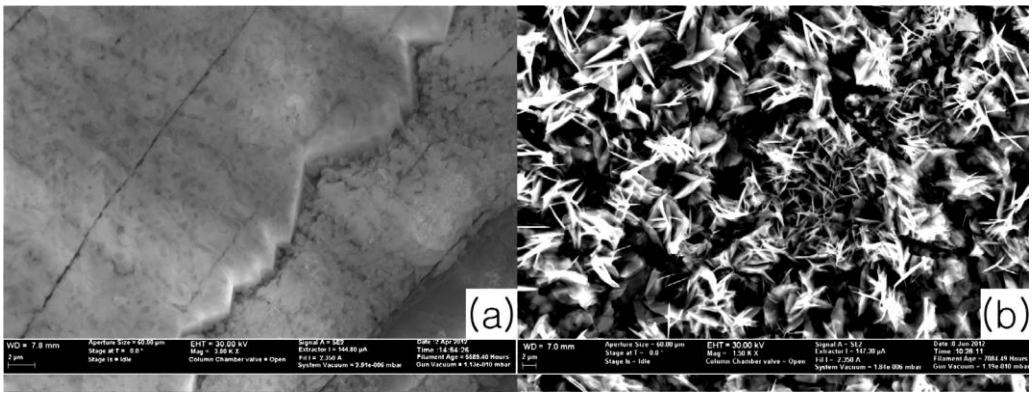


Figure 1-4 The nanostructure theory used in the first study; (a) a pure molten salt (b) the same molten salt of (a) with a formed nanostructure after doping nanoparticle [30].

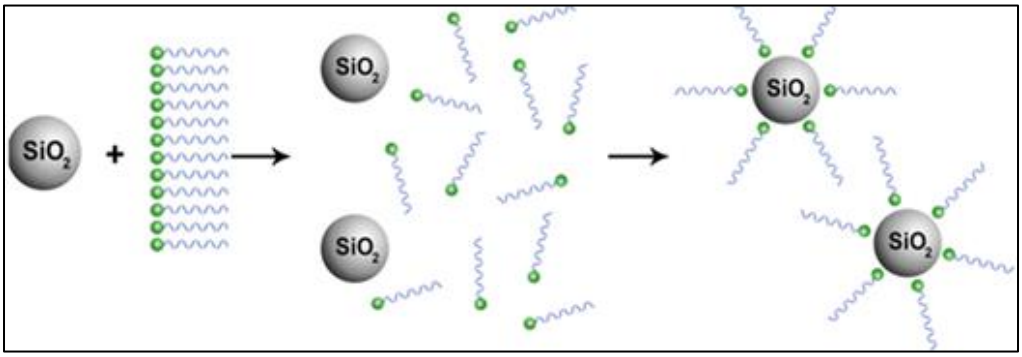


Figure 1-5 A representation of the anticipated in-situ superstructure formation by fabricated nano-additives for second study [68]

# Chapter 2

## First Study: Theoretical Study of specific heat capacity enhancement of molten salt nano-eutectic via nanostructural change

### *2.1. Specific heat capacity of nanostructure*

A molten carbonate salt eutectic $Li_2CO_3 - K_2CO_3$ doped with $SiO_2$ nanoparticles was used in this approach because the material characterization studies, such as transmission electron microscope (TEM) and scanning electron microscope (SEM) were available, and the experimental work was already done by other research groups [3], [40], [45].

First, we modified the conventional specific heat capacity model (equation 1) to replicate the effect of the nanostructure, as follows:

$$C_{nf} = m_{np}C_{np} + m_{ns}C_{ns} + (m_{bf} - m_{ns})C_{bf} \quad (2)$$

Where $ns$ represents nanostructure.

Here, to complete this equation, we need to estimate two unknowns, $m_{ns}$ and $C_{ns}$. However, measuring these values in an experiment is impossible with current technology. Hence, we used a simple image-processing tool (i.e., MATLAB) to approximate the amount of nanostructures formed by one salt ($m_{ns}$ ; $Li_2CO_3$) from the material characterization studies in the literature [3], [40], [45]. We used Wang et al. [2] equations to estimate the specific heat capacity of the nanostructures, $C_{ns}$ , in the same way Saeedian [66] and Chakraborty [63] reported. The results were then substituted into Equation 2 and compared with the reported measured values.

Selected nano-eutectic consists of 1 wt. % $SiO_2$ nanoparticles in a eutectic of $Li_2CO_3 - K_2CO_3$. The molar eutectic ratio is 62:38 ($Li_2CO_3$: $K_2CO_3$). The eutectic melting point of 488 °C [69] and the specific heat capacity is 1.6 $kJ/kg°C$ [70].

To calculate $C_{ns}$ , it is necessary to determine whether nanosturcture is $Li_2CO_3$ or $K_2CO_3$. Therefore, a material characterization was performed by a backscattered electron microscope (Zeiss Supra 55 VP, Carl Zeiss AG, Oberkochen, Germany). Figure 2-1 is a backscattered electron (BSE) microscopic image of $Li_2CO_3 - K_2CO_3$ , doped with $SiO_2$ nanoparticles. BSE microscopy is a very powerful tool used when to differentiate materials or phases. In BSE microscopy, the number of backscattered electrons from a sample is proportional to the average atomic number of the sample. Typically brighter areas have a greater average atomic number and darker areas have a lower average atomic number. In figure 2-1, needle-shaped nanostructures (red) seem less bright than nearby bulk material (blue), so, the needle-shaped nanostructures should be $Li_2CO_3$ (a lower average atomic number than $K_2CO_3$). Figure 2-1 (c) is a simple modeling of a needle-like nanostructure. We approximated that one needle-like nanostructure of figure 2-1 (b) can be represented by a chain of cubes.

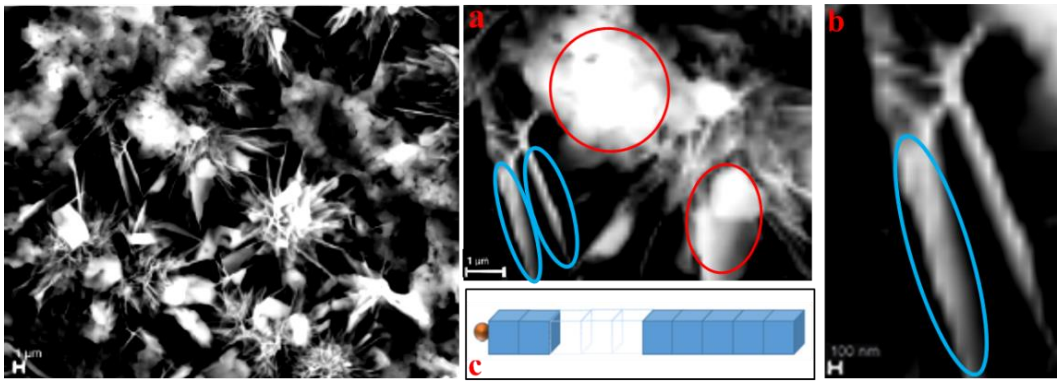


Figure 2-1 (a) $Li_2CO_3 - K_2CO_3$ doped with $SiO_2$ nanoparticle [47].

(b) These needle-like nanostructures (red) are less bright than the bulk (blue), indicating they are $Li_2CO_3$ (lower Z-value).

(c) A modeling of one long needle-shaped nanostructure formed on the nanoparticle surface

To calculate the specific heat capacity of a needle-like nanostructure, we followed Wang et al.'s calculation [2], which is for nano-sized particles and then extended it to a nanostructure model, as in figure 2-1 (c). Since the exact number of unit cells along each direction of the base vectors cannot be calculated for the fractal-like nanostructure, we modeled the nanostructures as a long cube consisting of several cubes with the same volume. The dimension of each cube was determined to be 100 nm × 100 nm × 100 nm to best approximate the structure in the backscattered image (Figure 2-1 (c)).

Based on the elastic continuum assumption, we combined the Einstein and Debye models. The Einstein angular velocity ($\omega_E$) and the Einstein temperature ($\theta_E$) were attained from the specific heat capacity equation of the bulk $Li_2CO_3$ as follows [2]:

$$C_{bulk} = \frac{3n.N.K_B}{\rho V_{crystal}} \left(\frac{\theta_E}{T}\right)^2 \frac{e^{\theta_E/T}}{\left(e^{\theta_E/T} - 1\right)^2}, \qquad \left(\omega_E = \frac{K_B \theta_E}{\acute{h}}\right) \tag{3}$$

The effective sound velocity ($\vartheta$) was determined by [2]:

$$\vartheta = \frac{K_B . \theta_D / \acute{h}}{\left(6\pi^2/\Omega\right)^{1/3}} \tag{4}$$

Where $K_B$ is Boltzmann's constant $(1.381 \times 10^{-23}\, J.K^{-1})$, $\theta_D$ is the Debye temperature of the bulk material, $\acute{h} = h/2\pi$ , $h$ is Planck's constant $(6.626 \times 10^{-34}\, J.s)$, $n$ is the number of atoms per unit cell of the material, $\rho$ is the density of the material (kg/m$^3$), Ω is the volume of a unit cell structure (A°$^3$), $V_{crystal}$ is volume (m$^3$) $(= N \times \Omega \times 10^{-30})$, $\theta_E$ is Einstein temperature (K), and T is variable temperature at which the specific heat capacity of bulk wish to be calculated (K).

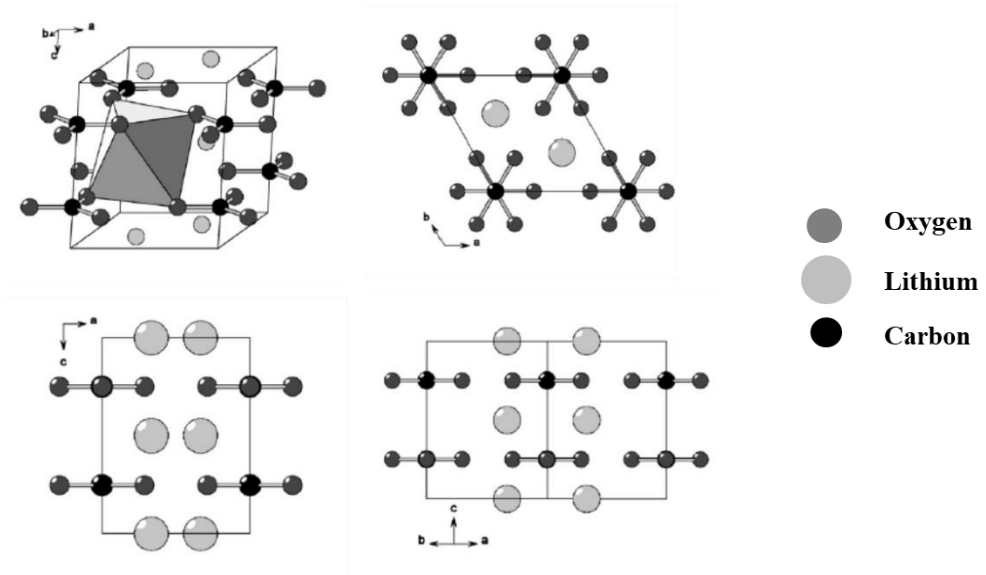


Figure 2-2 Crystal structure of the $Li_2CO_3$ (P$6_3$=mcm) [71]

The nanostructure model in figure 2-1 (C) consists of multiple cubes, and the specific heat capacity of each cube was calculated according to Wang and others' approach. First, The number of surface atoms to the total number of atoms in a cube was approximated as $x = {N_a}^s/N_a$ [2], where ${N_a}^s$ is the number of surface atoms, and $N_a$ is the total number of atoms in each cubic nanostructure.

The size of the base vectors of the reciprocal lattice unit cell, which are related to its base vectors, and volume is calculated as follows [2]:

$$\overrightarrow{b_1} = \frac{2\pi(\vec{b} \times \vec{c})}{\Omega}, \qquad \overrightarrow{b_2} = \frac{2\pi(\vec{a} \times \overrightarrow{c})}{\Omega}, \qquad \overrightarrow{b_3} = \frac{2\pi(\vec{a} \times \overrightarrow{b})}{\Omega} \tag{5}$$

Where $\vec{a}, \vec{b}, \vec{c}$ are based vectors of the unit cell, $\overrightarrow{b_1}, \overrightarrow{b_2}, \overrightarrow{b_3}$ are base vectors of reciprocal lattice of the unit cell. The mean vibration of frequency is determined by a simple mixing rule of the vibrations of surface and interior atoms as follows [2]:

$$\bar{\omega}_E = xL\omega_E + (1 - x)\omega_E \tag{6}$$

Where $L = \sqrt{Z^s/Z}$ is the softening factor, $Z^s$ and $Z$ are the number of interior atoms bonding, and the average number of surface atoms, respectively [2].

The specific heat capacity of bulk $Li_2CO_3$ was calculated by the following formula lithium carbonate [72]:

$$C_{bulk\ Li_2CO_3} = A + B.T + C.T^2 + D.T^3 + {}^{E}/_{T^2} \quad (7)$$

Where A, B, C, D, and E are constants; A= 68.3323, B= 146.639, C= -162.57, D= 248.026, and E= -0.702297 for bulk $Li_2CO_3$.

Table 2-1 shows crystal structure data, thermodynamic and quantum properties of $Li_2CO_3$, and other parameters used in the specific heat capacity calculation.

According to Wang et al. [2], since the effect of the surface atoms cannot be neglected in nanometer-sized particles, the specific heat capacity consists of an acoustic part from the Debye model and an optical part from the Einstein model as follows:

$$C = C_{Optical} + C_{\text{Acoustic}} \quad (8)$$

$$C_{Optical} = \frac{(3n-3)N}{\rho V_{crystal} K_B T^2} \frac{(\acute{h}\bar{\omega}_E)^2 e^{\hbar\bar{\omega}_E/(K_B T)}}{(e^{\hbar\bar{\omega}_E/(K_B T)} - 1)^2} \quad (9)$$

$$C_{v,Acoustic} = \frac{3}{\rho V_{crystal} K_B T^2} \left( \sum_{\vec{q}\in Q^I} \frac{(\acute{h}\vartheta q)^2 e^{\hbar\vartheta q/(K_B T)}}{(e^{\hbar\vartheta q/(K_B T)} - 1)^2} + \sum_{\vec{q}\in Q^S} \frac{(\acute{h}L\vartheta q)^2 e^{\hbar L\vartheta q/(K_B T)}}{(e^{\hbar L\vartheta q/(K_B T)} - 1)^2} \right) \quad (10)$$

$$Q^I = \{\vec{q}| - (N_i^I/2) < l_i \leq (N_i^I/2)\}, \qquad N_i^I = xN_i, i = 1,2,3 \quad (11)$$

$$Q^S = Q - Q^I, Q = \{\vec{q}| - (N_i/2) < l_i \leq (N_i/2)\}, i = 1,2,3 \quad (12)$$

where $\vec{q}$ is the elastic wave vector and expressed as:

$$\vec{q} = \frac{l_1}{N_1}\overrightarrow{b_1} + \frac{l_2}{N_2}\overrightarrow{b_2} + \frac{l_3}{N_3}\overrightarrow{b_3} \quad (13)$$

and $l_1, l_2, l_3$ are integrals, $N_1, N_2, N_3$ are the number of unit cells along the directions of the base vector.

Table 2-1 Crystal structure data of $Li_2CO_3$

| | |
|---|---|
| Unit cell structure [59] | Monoclinic |
| $n$, Number of atoms per unit Cell [59] | 24 |
| $a$ ($A°$), Dimension [59] | 8.39 |
| $b$ ($A°$), Dimension [59] | 5 |
| $c$ ($A°$), Dimension [59] | 6.21 |
| $\alpha = \gamma$ (°) [59] | 90 |
| $\beta$ (°) [59] | 101.32 |
| $N_1, N_2, N_3$ Number of the unit cell in each direction | 197 |
| $N$, Total number of unit cell per nanostructure | 7677263 |
| $\Omega$, Volume of the unit cell ($A°^3$) | 255.44 |
| $V_{Cubic,ns}$, Volume of each cubic nanostructure ($100nm^3$) ($m^3$) | $1 \times 10^{-21}$ |
| $V_{crystal}$ ($m^3$) | $1.961 \times 10^{-21}$ |
| $\rho$ ($kg/m\text{^}3$) [69] | 2090.73 |
| $\omega_E$, Einstein angular velocity ($1/s$) | $7.897 \times 10^{13}$ |
| $\theta_E$, Einstein temperature (K) | 603 |
| L (softening factor) | 0.1128 |
| $\vartheta$, Effective sound velocity ($m/s$) | 8004.5 |

### *2.2. Estimation of mass fraction of the nanostructure*

The next unknown value from Equation 2 is the mass fraction of the nanostructure, $\mathrm{m}_{\mathrm{ns}}$. As mentioned above, the mass fraction measuring in an experiment is impossible with current technology. Hence, we used a simple image-processing tool (i.e., MATLAB) to approximate the amount of $Li_2CO_3$ nanostructures from available material characterization study in the literature [3]. Each SEM image was converted to a binary image and the number of nanostructure pixels was compared with the total number of pixels to approximate the volumetric concentration of the nanostructure. Then, the numbers were multiplied by corresponding density values to calculate the mass fraction of the nanostructure. It is worth noting that these image analyses were done on images of the surface of each sample and thus they may not completely reflect the actual volumetric concentration of $Li_2CO_3$ nanostructures.

Figures 2-3 through 2-6 show the results of the image analyses.

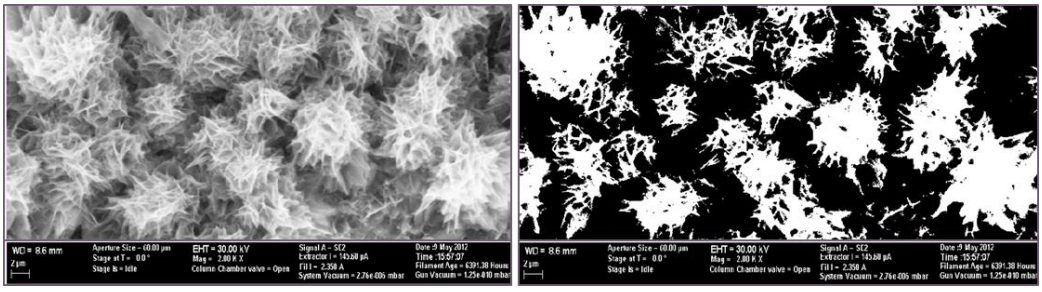

Figure 2-3 An image processing of the material characterization in literature [3] $Li_2CO_3 - K_2CO_3$ doped with $SiO_2$ 5nm nanoparticle by MATLAB. 3,241 nanostructure pixels out of the total 7865 pixels. The calculated mass fraction of the nanostructure is 38%.

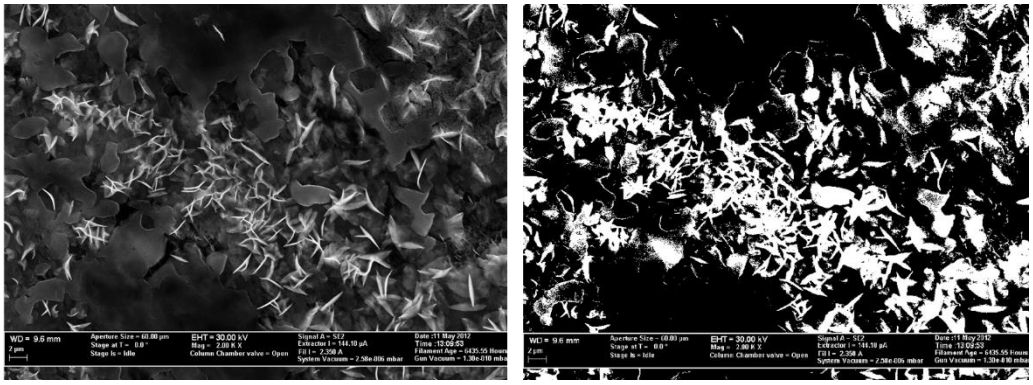

Figure 2-4 An image processing of the material characterization in literature [3] $Li_2CO_3 - K_2CO_3$ doped with $SiO_2$ 10nm nanoparticle by MATLAB. 1952 nanostructure pixels out of the total 5766 pixels. The calculated mass fraction of the nanostructure is 34%.

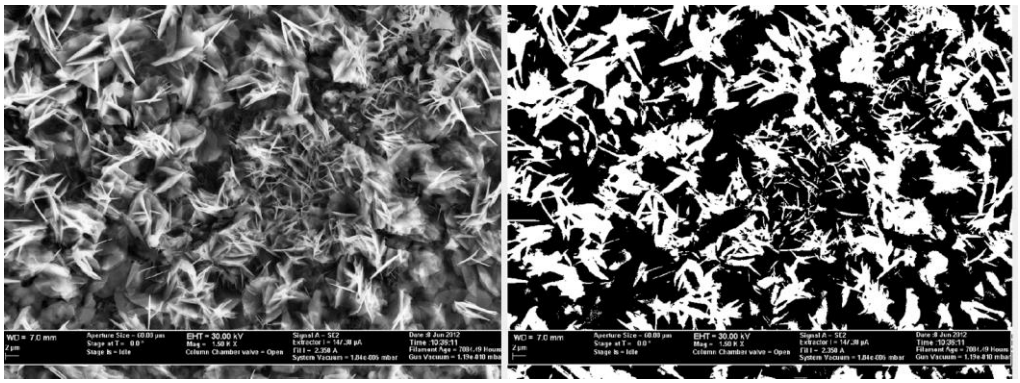

Figure 2-5 An image processing of the material characterization in literature [3] $Li_2CO_3 - K_2CO_3$ doped with $SiO_2$ 30nm nanoparticle by MATLAB. 2904 nanostructure pixels out of the total 4961 pixels. The calculated mass fraction of the nanostructure is 37%.

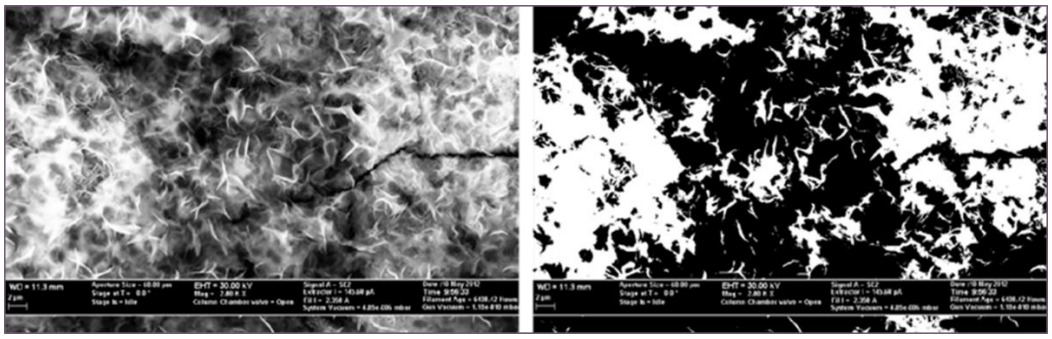

Figure 2-6 An image processing of the material characterization in literature [3] $Li_2CO_3 - K_2CO_3$ doped with $SiO_2$ 60nm nanoparticle by MATLAB. 3327 nanostructure pixels out of the total 4537 pixels. The calculated mass fraction of the nanostructure is 40%.

### *2.3. Results and discussion*

Using the data in table 2-1, the optical part (Equation 8) and the acoustic part (Equation 9) were calculated using MATLAB software (version R2017a, MathWorks Inc., Natick, MA). Tables 2-2 through 2-5 show the approximated mass fractions along with final value for the specific heat capacity of nanofluid. The mass fraction from the different sizes of the $SiO_2$ nanoparticle (5nm, 10nm, 30nm, 60nm) have been calculated to be 38%, 34%, 37% and 40%, respectively. Using this value together with the calculated specific heat capacity of the $Li_2CO_3$ nanostructure, the prediction by Equation 2 on the effective specific heat capacity of the molten salt nano-eutectic is calculated (Table 2-2 – 2-5). The error for the measured specific heat capacity from the literature [3] and the prediction by Equation 2 is only 2.0~4.0 %, which could be because of several factors, such as the image processing error and the estimation of a cubic nanostructure. Since the error is very small, it proves that our modified model can predict the specific heat capcity of the nanofluids, while model 1 presented in the introdcuction section could not predict the enhancement of specific heat capacity in the molten salt nanofluids.

Our modified model takes the nanostructure theory into account, and as shown in tables 2-2 through 2-5, it is able to successfully validate the experimental result, which proves the existence of the nanostructures and that such nanostructures are responsible for the specific heat capacity enhancement.

Table 2-2 A comparison between the theoretical estimate and the experimental value for $Li_2CO_3 - K_2CO_3$ doped with 5nm $SiO_2$ nanofluid

| | |
|---|---|
| Specific heat capacity of $Li_2CO_3 - K_2CO_3$ eutectic [70] | 1.60 $kJ/kg°C$ |
| Specific heat capacity of $SiO_2$ nanoparticle [73] | 1.25 $kJ/kg°C$ |
| Specific heat capacity of calculated $Li_2CO_3$ nanostructure | 2.64 $kJ/kg°C$ |
| The estimated mass fraction of $Li_2CO_3$ nanostructure | 38 % by weight |
| Mass fraction of $SiO_2$ nanoparticle | 1.0 % by weight |
| Specific heat capacity prediction by Equation 2 | 1.99 $kJ/kg°C$ |
| Experimental specific heat capacity value [26] | 1.97 $kJ/kg°C$ |
| The error between Equation 2 and the measured value | 2.0% |

Table 2-3 A comparison between the theoretical estimate and the experimental value $Li_2CO_3 - K_2CO_3$ doped with 10nm $SiO_2$ nanofluid

| | |
|---|---|
| Specific heat capacity of $Li_2CO_3 - K_2CO_3$ eutectic [70] | 1.60 $kJ/kg°C$ |
| Specific heat capacity of $SiO_2$ nanoparticle [73] | 1.25 $kJ/kg°C$ |
| Specific heat capacity of calculated $Li_2CO_3$ nanostructure | 2.64 $kJ/kg°C$ |
| The estimated mass fraction of $Li_2CO_3$ nanostructure | 34 % by weight |
| Mass fraction of $SiO_2$ nanoparticle | 1.0 % by weight |
| Specific heat capacity prediction by Equation 2 | 1.95 $kJ/kg°C$ |
| Experimental specific heat capacity value [26] | 2.01 $kJ/kg°C$ |
| The error between Equation 2 and the measured value | 4.0 % |

Table 2-4 A comparison between the theoretical estimate and the experimental value $Li_2CO_3 - K_2CO_3$ doped with 30nm $SiO_2$ nanofluid

| | |
|---|---|
| Specific heat capacity of $Li_2CO_3 - K_2CO_3$ eutectic [70] | 1.60 $kJ/kg°C$ |
| Specific heat capacity of $SiO_2$ nanoparticle [73] | 1.25 $kJ/kg°C$ |
| Specific heat capacity of calculated $Li_2CO_3$ nanostructure | 2.64 $kJ/kg°C$ |
| The estimated mass fraction of $Li_2CO_3$ nanostructure | 37 % by weight |
| Mass fraction of $SiO_2$ nanoparticle | 1.0 % by weight |
| Specific heat capacity prediction by Equation 2 | 1.98 $kJ/kg°C$ |
| Experimental specific heat capacity value [26] | 1.95 $kJ/kg°C$ |
| The error between Equation 2 and the measured value | 2.0% |

Table 2-5 A comparison between the theoretical estimate and the experimental value $Li_2CO_3 - K_2CO_3$ doped with 60nm $SiO_2$ nanofluid

| | |
|---|---|
| Specific heat capacity of $Li_2CO_3 - K_2CO_3$ eutectic [70] | 1.60 $kJ/kg°C$ |
| Specific heat capacity of $SiO_2$ nanoparticle [73] | 1.25 $kJ/kg°C$ |
| Specific heat capacity of calculated $Li_2CO_3$ nanostructure | 2.681 $kJ/kg°C$ |
| The estimated mass fraction of $Li_2CO_3$ nanostructure | 40 % by weight |
| Mass fraction of $SiO_2$ nanoparticle | 1.0 % by weight |
| Specific heat capacity prediction by Equation 2 | 2.01 $kJ/kg°C$ |
| Experimental specific heat capacity value [26] | 2.0 $kJ/kg°C$ |
| The error between Equation 2 and the measured value | 2.0% |

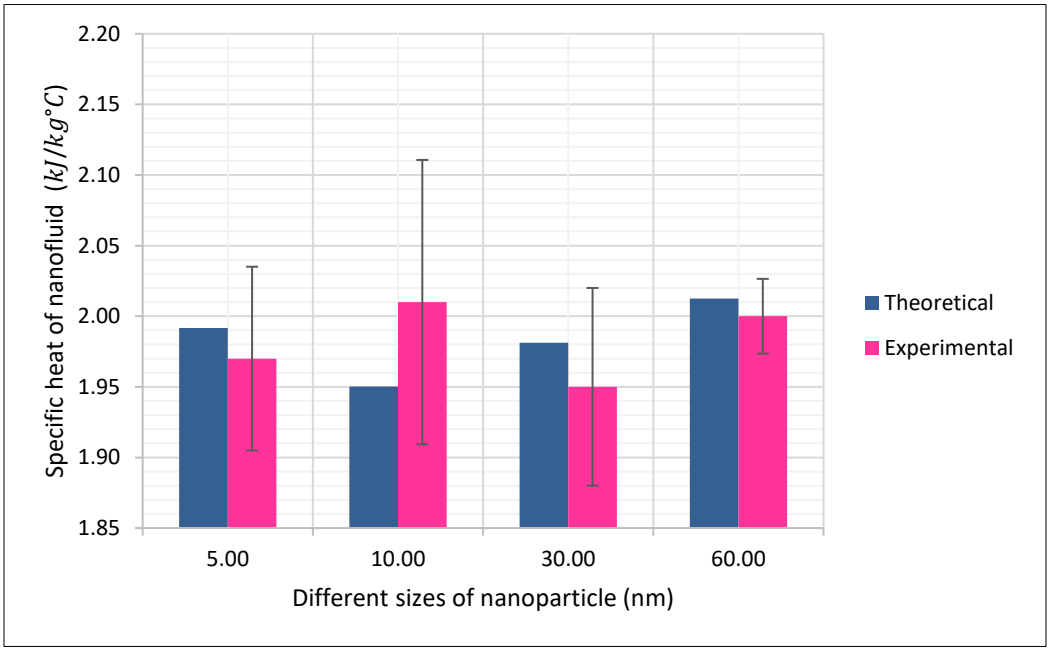


Figure 2-7 A comparison between the different size of nanoparticles effect on nanofluid specific heat capacity

# Chapter 3

## Second study: Experimental study of enhanced thermo-physical properties via polyalphaolefin superstructure

### *3.1. Polyalphaolefin characteristics*

Polyalphaolefin (PAO) was industrialized in the 1930s and became one of the first commercial engine oils in 1970s. PAO is one of the synthetic hydrocarbon liquids manufactured from the monomer ethylene $H_2C = CH_2$. Polyalphaolefins have a very complicated branched structure that has an olefin bond in the alpha position of one of the branches. PAO is cosidered to be a polymer created by polymerizing an alpha-olefin. They are catagorized at API Group IV and are a 100% synthetic chemical compound.

Olefin-carbons saturated with hydrogen are called hydrogenated polyalphaolefins. These compounds offer excellent thermal stability to the molecule. Synthetic-base fluids (comparable to oil muds) are created with numerous types of synthetic liquids. PAO is a 100% synthetic base oil used in the production of high-performance lubricants. PAO typically has a higher viscosity index than mineral oils and better oxidative stability (i.e., they are less likely to break down).

PAOs are made uniquely from alpha olefins. Alpha-olefins (or α-olefins) are organic compounds, which means they are alkenes (also known as olefins) with the chemical formula of $C_xH_{2x}$, differentiated by having a double bond at the alpha (α) position [74]. Such a position of a double bond increases the reactivity of the compound and causes a beneficial effect on its applications.

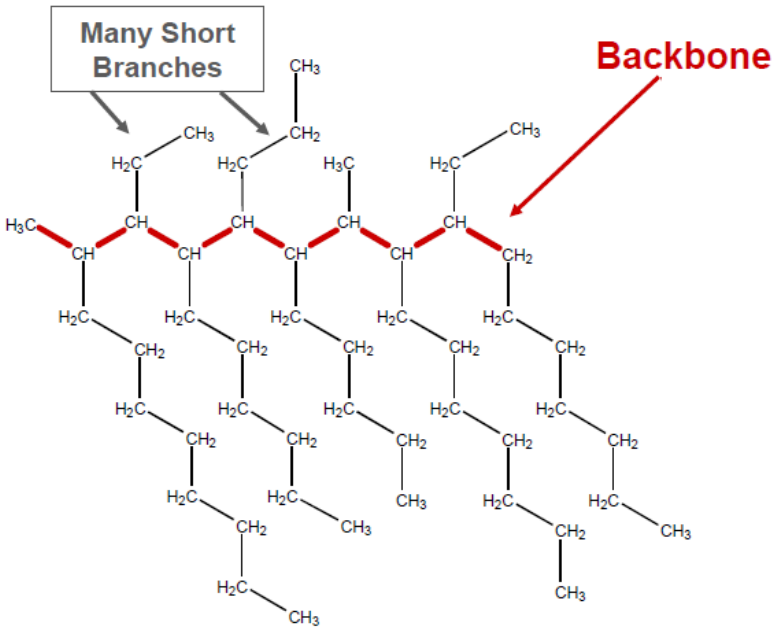


Figure 3-1 Conventional PAO structure [75]

Polyalphaolefin does not include ring structures, sulfur, double bonds, waxy hydrocarbons, or nitrogen components. Therefore, it is known as a very non-polar base oil. PAOs have many advantages over mineral oils; 1) excellent low-temperature flow, 2) pour point features, 3) compatibility with mineral oils, seals, and paints mainly found in lube oil systems, and 4) excellent oxidation stability.

Since the PAOs have a very controlled structure, they do not have lighter, more unstable and explosive hydrocarbons.

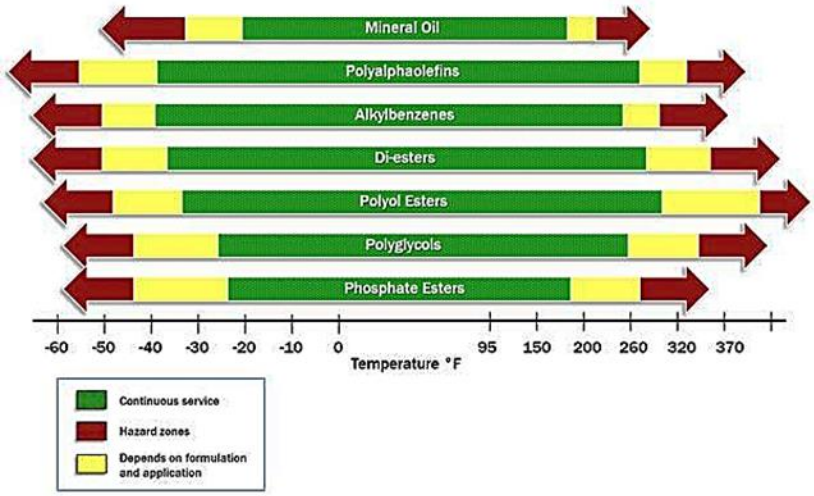


Figure 3-2 Base Oil Types vs. Service Temperature Range [75]

### *3.1.1. Applications of Polyalpholefin*

Aviation & Aeronautics: Since the PAOs have high flash and fire points, they have been used as hydraulic fluids in aircraft, as the result of having a very high degree of safety if a hydraulic leak happens. PAOs are considered to have lubricity and viscosity over a wide range of temperatures without any breakdown.

Industrial: excellent thermal stability, lower friction coefficient, and outstanding heat-transfer capabilities of PAO will help to reduce the friction and advance the compressor productivity. PAOs will also help the rotary compressors to operate continuously for up to 8,000 hours. The low volatility of the PAO will help to decrease the make-up consumption by 30% in comparison to other conventional oils.

Military: PAOs have been used widely for military application, so they have been field-tested to test the capacity of the PAOs. The positive results of PAO have allowed the military industry to push the limits for their extremely high-tech equipment, such as the Abrams M-1A tank and the Falcon F-22 fighter jet. PAOs have been used for heavy-

duty engine oils, greases, hydraulic systems and gearbox oils in military applications to keep complicated equipment operating even in very harsh environments. PAOs have very excellent dielectric properties, so they have been used as a coolant in military avionics systems.

Environmental: In places where the environmental considerations are a concern for offshore drilling and production applications, the thermal stability characteristic of PAOs offers notable downhole operation in those applications. The same characteristics of PAOs are also advantageous in other environmentally sensitive regions such as rainforests or wetlands. Similarly, because of the biodegradable characteristic of PAOs, they can be a suitable replacement for vegetable-based oils, removing the performance problems associated with this type of product repeatedly.

Transportation: PAOs are considered to operate under the extreme conditions of today's high-torque, smaller engines and the addition of sophisticated equipment such as multiple valves and supercharges. Since quality and reliability are paramount in transmission fluids, PAOs are a good candidate for the transmission fluids. The excellent oxidative stability of the PAOs permits truck or car transmissions to be "filled for life," which results in much fewer service costs and maintenance while drastically decreasing downtime for expensive industrial vehicles.

### 3.2. *Polyethylene-block-poly (ethylene glycol) characteristics*

Polyethylene-block-poly (ethylene glycol) (PBP) is a nonionic surfactant, which has a linear formula of $CH_3CH_2(CH_2CH_2)_m(OCH_2CH_2)_nOH$. The PBP used in this research has the average molecular weight (MW) of 1400, with 50 wt. % of ethylene oxide and a melting point of 115℃.

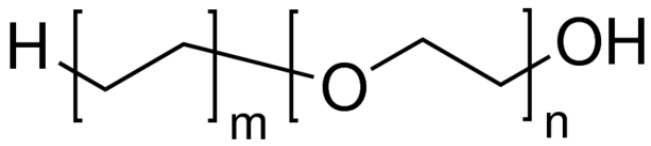


Figure 3-3 PBP structure

PBP is a condensation polymer and is useful for biological, chemical, and pharmaceutical applications and can be used as detergents and designer surfactants. PBP can be readily manufactured by the anionic ring opening polymerization of ethylene oxide into arrays of molecular weights and different versions groups [76].

### *3.3. Materials*

Polyethylene-block-poly (ethylene glycol) [avarage MW ca. 1,400] (termed as "PBP") and $SiO_2$ nanoparticles were used to form an artificial nanostructure on the nanoparticle surface. Precisely, we predicted that dispersing the fabricated nano-additives, which are PBP in our case, along with the nanoparticles into the PAO can begin the in-situ formation of the superstructure. Such a superstructure performs similarly as the fractal-like (needle-shaped) nanostructures of molten salt nanofluids, resulting in the enhanced specific heat capacity of PAO, as previosly discussed in the proposed synthesis illustrated as a simple schematic in Figure 1-5. The PAO-68 was acquired by Behr Hella service (Schwaeblisch, Germany), and the $SiO_2$ nanoparticles (10 nm;

amorphous) were purchased from Meliorum Technology, Inc and the polyethylene-Block-Poly was bought from Sigma Aldrich.

### *3.4. Methods*

The following is the general process for preparing the nanofluid sample: 98 wt. % Polyalphaolefin-68, 1 wt. % Polyethylene-Block-Poly (Ethylene Glycol), and 1 wt. % $SiO_2$ nanoparticle (size of the 10nm) were specifically measured on a Sartorius CPA225D microbalance and mixed together in a glass vial (25 ml). The PBP has been grinded manually for 5 minutes in advance for homogenousity and a better dispersion. We used the 1% nanoparticle concentration by weight to keep the consistensy with the previous reports [3], [33], [34], [38]–[42]. A Branson 3510 sonicator (purchased from Branson Ultrasonics Corporation) used for sonicating the samples for 200 minutes ensured an even more homogeneous dispersion of sample materials inside the glass vial. Figure 3-4 shows the pure PAO and the nanofluid after sonication step. The actual nanoparticle size measurement is shown in figure 3-5, which has been measured by a photon correlation spectroscopy.

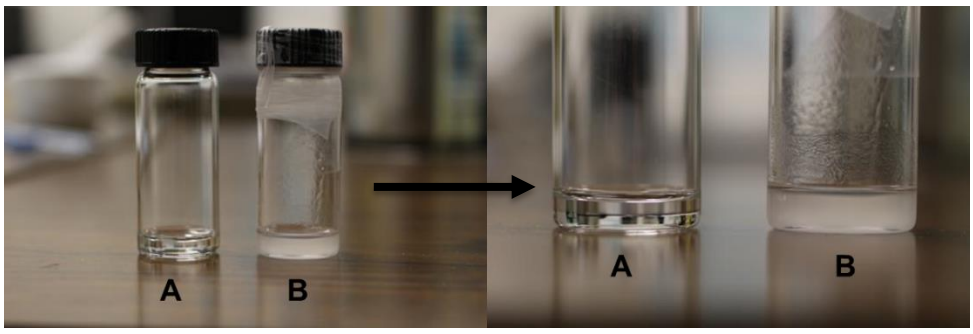


Figure 3-4 Pure PAO (A) vs. the nanofluid (B)

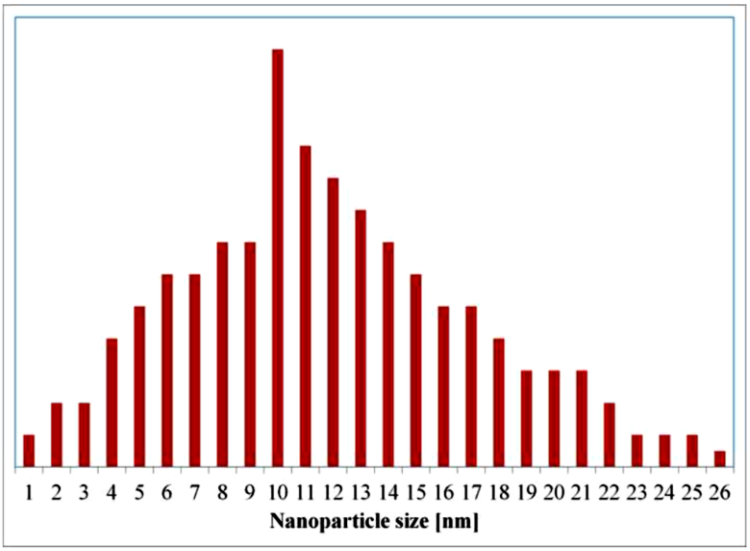


Figure 3-5 Nanoparticle size distribution by photon correlation spectroscopy.

### *3.5. The measurement procedure of the specific heat capacity*

1000 mg of PAO-superstructure was prepared and measured on the microbalance, which includes 10 mg of PBP (1 wt. %), 10 mg of $SiO_2$ nanoparticle (1 wt. %), and 980 mg of PAO-68. 1000 mg of PAO was prepared to get the value for pure PAO and to use it as a reference and comparison to nanofluid. Another sample prepared for measurements contained the pure PAO (99 wt. %; 990 mg) and $SiO_2$ nanoparticle (1 wt. %; 10 mg) to confirm whether there is a direct effect of $SiO_2$ nanoparticles on the specific heat capacity of PAO; such a control experiment is very valuable to prove that the enhancement in the specific heat capacity by dispersing the nanoparticles can only spontaneously happen in molten salts as a result of the salt molecules forming the unique nanostructure. To show and prove the effect of the PBP on the PAO, the same sample was prepared of the pure PAO (99 wt. %; 990 mg) and $SiO_2$ nanoparticle (1 wt. %; 10 mg). A modulated differential calorimeter (Q20, TA Instruments, Inc.) measurement was conducted to measure and analyze the specific heat capacity of every prepared sample.

Tzero hermetic aluminium pans / lids were used to pour each sample into it to ensure no sample loss during the specific heat capacity measurement. The weight of all the samples was measured on the microbalance before and after each experiment of DSC to guarantee there would be no mass loss. The pan and lid of every sample was disposed after each experiment in order to confirm that there is no contamination between each sample and the measurement cell inside the DSC. For all the tests, the DSC curve was checked and monitored to prove that there would be no moisture effect or no chemical reaction during the specific heat capacity measurements.

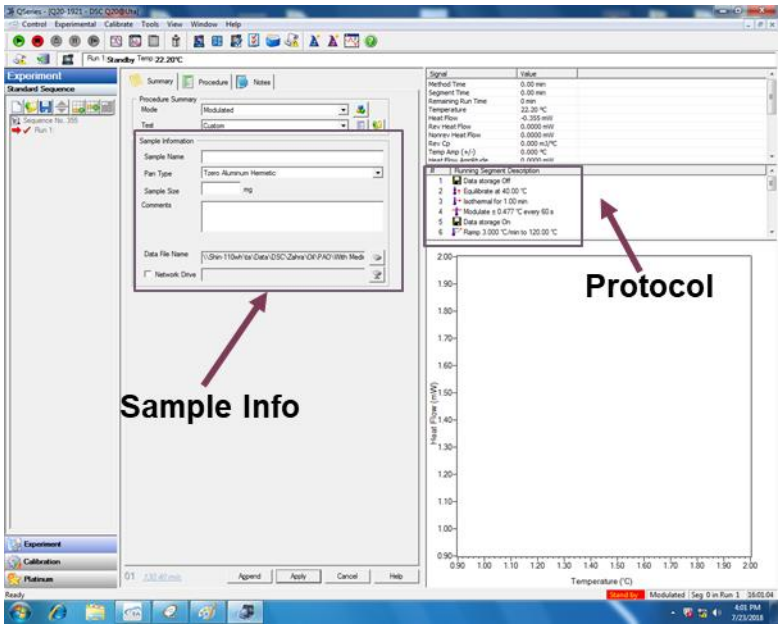


Figure 3-6 Q series TA instrument of DSC interface

### *3.6. The measurement procedure of the thermal conductivity*

Pure PAO and the PAO nanofluid were prepared in the amount of 4000 mg of each to measure thermal conductivity. The very first experiment was conducted for measuring the thermal conductivity of the pure PAO to get the reference value for the followed measurements. A chamber consisting of two halves was used for thermal conductivity experiments. After pouring the pure PAO into the test chamber, the upper half of the chamber was posited over it. The testing chamber was placed into an “OV-11” furnace (Jeio Tech, Inc) afterward with a constant temperature set at 120°C. The flanges of the lower part of the chamber were fixed to the upper part. Both parts of the chamber then were jointed with Allen screws. The test chamber has eight holes on top for the eight thermocouples to be inserted into the chamber. All eight thermocouples were then connected to an NI SCXI 1000 Data Acquisition System (National Instruments, Inc). There is also one more thermocouple connected only to the DAS to be put into the furnace to measure the temperature of the furnace continuously. Another central hole on top of the test chamber is where the hot wire was inserted. One end of the hot wire was connected to a E3644A DC power source (Keysight Technologies company), and the other end was attached to a DAS. To measure the voltage drop in the hot wire, the tapping has been done into the hotwire and then the hot wire connected with the DAS. The testing chamber was held in the furnace for two hours to stabilize the temperature of the chamber and the sample and to have a steady state before starting the experiment. After stabilization, the DC power supply and the DAS was turned on to run the experiment. The power supply of 12V DC, with the current value of 2.56 A, was set for the experiments. To store the data, a LabVIEW program was used. After stabilization and running the power supply, the LABVIEW began to run, and the thermal conductivity of both pure and nanofluid PAO samples was measured.

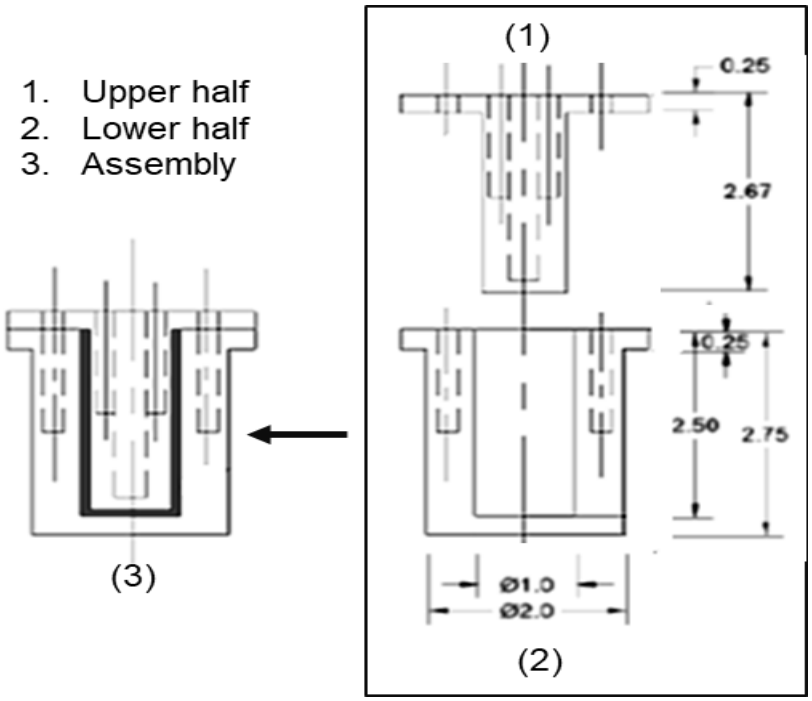


Figure 3-7 Test chamber cross section diagram

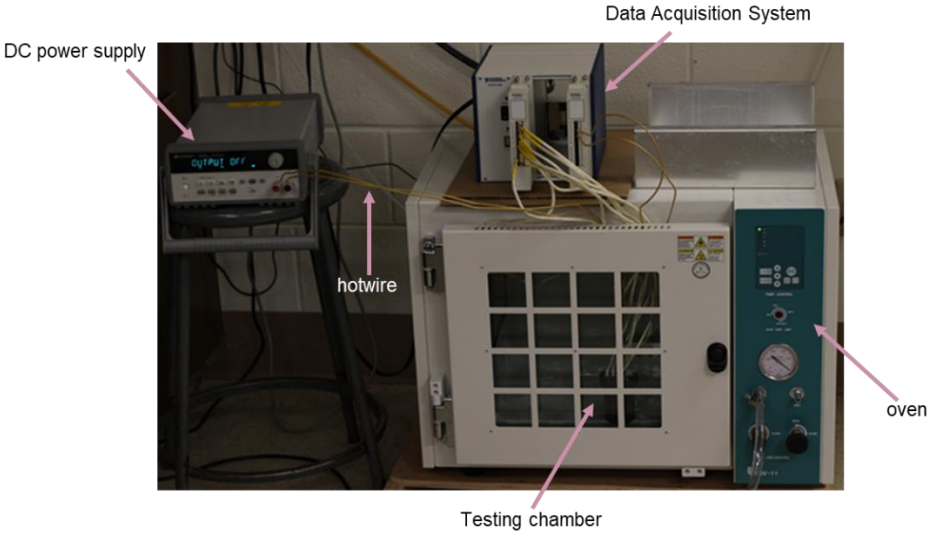


Figure 3-8 In lab-built apparatus for thermal conductivity measurement

*3.6.1. The mechanism of the in-lab built apparatus for thermal conductivity:*

A very standard method (in the steady state) for evaluating the thermal conductivity of the nanofluids is the cylindrical cell method, which has high speed and accuracy of measurements. In this method, a stainless steel testing chamber with two parts is a standard way to utilize the measurements with the halves including the concentric cylinders. The pure PAO, or the nanofluid, was poured into the ring-shaped gap that is between the two cylinders for every experiment. A hot wire was inserted in the center of the smaller half (the inner part of the testing chamber), and then slits were cut across the glass fiber insulation up to where the hot wire was put inside the inner part of the testing chamber so that the hotwire could be exposed to the bare stainless steel. The slits of the other end of the hotwire were attached to the DAS with another wire for voltage drop measurements. The slits of the bottom ends of the hot wire were attached to the DC power supply. After turning the power supply on, the electric resistance on the wires of the hot wire emitted heat and heated the hotwire up. The heat flux had a radial direction from the hot wire, towards the sample inside the test chamber. The eight calibrated K- type thermocouples inside the holes of the test chamber measured the temperature at various radial direction points. [77].

The following is the thermal conductivity of the nanofluid calculated using Fourier's equation,

$$R = \frac{\Delta T}{Q} = \frac{\ln \frac{r_2}{r_1}}{2\pi k l} \tag{14}$$

For inner and outer concentric cylinder, we have:

$$R_{in,cyl} = \frac{\ln \frac{r_2}{r_1}}{2\pi l K_{inner\ steel}} \tag{15}$$

$$R_{out,cyl} = \frac{ln\frac{r_3}{r_2}}{2\pi l K_{outer\ steel}} \tag{16}$$

In addition, for nanofluid:

$$R_{nf} = \frac{\ln\frac{r_4}{r_3}}{2\pi l K_{nanofluid}} \tag{17}$$

Substituting in equation (14) we have:

$$\frac{(T_{in} - T_{out})}{Q} = \frac{\ln\frac{r_2}{r_1}}{2\pi l K_{inner\ steel}} + \frac{ln\frac{r_3}{r_2}}{2\pi l K_{outer\ steel}} + \frac{\ln\frac{r_4}{r_3}}{2\pi l K_{nanofluid}} \tag{18}$$

From that, we can get the thermal conductivity of nanofluid:

$$K_{nanofluid} = \frac{ln\frac{r_3}{r_2}}{2\pi l K_{steel}(\frac{(T_{in} - T_{out})}{Q} - \ln\frac{r_2}{r_1} - \ln\frac{r_4}{r_3})} \tag{19}$$

Where $T_{in,1}, T_{in,2}, T_{in,3}, T_{in,4}$ are the temperatures measured by the four inner thermocouples and $T_{out,1}, T_{out,2}, T_{out,3}, T_{out,4}$ are the temperatures measured by the four outer thermocouples. $r_1$ is the radial distance of the each four inner thermocouples from the central axis of the test chamber, $r_2$ is the outer radius of the inner cylinder, $r_3$ is the inner radius of the outer cylinder and $r_4$ is radial distance of the each four outer thermocouples from the central axis of the test chamber, $R$ is the thermal resistance.

### *3.7. The measurement procedure of the viscosity*

To measure the viscosity, 2000mg pure PAO and 2000mg PAO nanofluid were prepared. The discovery of hybrid rheometer (HR-1) was used to conduct the experiments. As you see in figure 3-12, the rheometer has a cone-plate geometry which is connected to a spindle drive. The pure PAO or the nanofluid was poured into the cup below the bob. After running the rheometer, the bob rotates, and it measures the different drag of the nanofluid or the pure PAO. The rheometer is connected to a computer using the software Trios V.3.3.1.4246 to store and analyze the data. Before starting any experiments, the rheometer has to be calibrated. The protocol used for our experiments consisted of 1-hour of soaking time for both flows sweeps with a constant temperature of 120°C.

Figure 3-9 a) Discovery Hybrid Rheometer (HR-2)

b) Cone shaped geometry and the plate to pour samples inside

# Chapter 4

## Experimental results and discussions

### *4.1. Specific heat capacity*

The results of specific heat capacity measurements are given in figures 4-3 through 4-6 and table 4-1. In figure 4-3 the specific heat capacity measurements of pure PAO and PAO + $SiO_2$ nanoparticle (1 wt. %) are shown together with the estimation by the conventional specific heat capacity model (Equation 1).

The very low nanoparticle concentration (~1% by weight) was also a factor in causing the estimation by the model (1) to significantly agree with the experimental results. The result presents no major enhancement in the specific heat capacity (Figure 4-3). Many researchers [45], [58] reported that the specific heat capacity enhancement by doping the nanoparticles happens only for molten salt nanofluids, but the conventional specific heat capacity model (Equation 1) could not predict this enhancement, but it agrees with the experimental data for conventional nanofluids. This model also validates the very recent research [58] that specific heat capacity enhancement doped with nanoparticles does not happen for PAO medium (i.e., non-salt based nanofluid).

Figure 4-1 shows the mechanism of the specific heat capacity enhancement for our proposed superstructure formation. This type of structure was introduced molten salt nanofluids, liquid structures, etc. where the amphiphiles are acting similarly to PBP, as shown in figure 4-2, fabricated nanoparticles could have several possible mechanisms in which the amphiphile is acting like the PBP in our study.

It is important to mention that to the extent of our best knowledge the mechanism of specific heat capacity mechanism for conventional nanofluid was not studied before,

and our proposed mechanism in figure 4-1 is the first idea presented to be responsible for specific heat capacity enhancement.

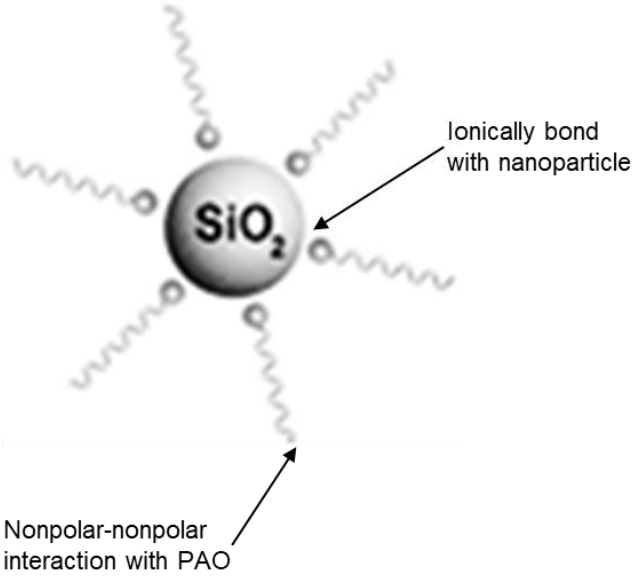


Figure 4-1 Proposed mechanism for enhanced specific heat capacity enhancement

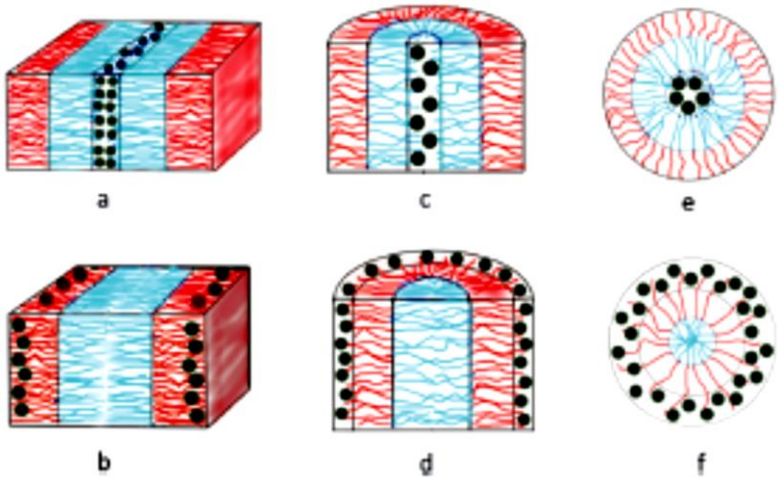


Figure 4-2 Schematic representation of amphiphiles forming the nanoparticles structures (a) and (b) lamellar structure; (c) and (d) cylindrical structure; (e) and (f) spherical structure. The lines are amphiphile, and the dots are nanoparticles. (amphiphile is acting like PBP in our case) [78]

Figure 4-4 presents the DSC results for pure PAO and the fabricated nanostructure (hydroxy-ended poly (Polyethylene-Block-Poly 1,400) at 1 wt. % concentration. The result shows that the PBP caused a slight enhancement in specific heat capacity (~20%) with a significant variation in the measurements. Such variation comes from the possibly agglomerated pre-fabricated PBP in the mixture.

In figure 4-5 the PAO and PAO + $SiO_2$ nanoparticles (1 wt. %) + PBP (1 wt. %) is presented in the first thermal cycle. All the DSC results showed a linear increase of specific heat capacity with temperature. In the first thermal cycle, the dispersed PBPs are predicted to ionically bond to the nanoparticles to form the superstructure.
The small peak near 100 °C specifies that the bonding procedure occurs in the first thermal cycle (over 100 °C).

The specific heat capacity results of pure PAO and PAO + $SiO_2$ nanoparticles (1 wt. %) + PBP (1 wt. %) are shown in figure 4-6. These are the results after the first DSC thermal cycling test (therefore, the PBP are already bonded wholly to nanoparticles). All six samples have shown significant enhancement in the specific heat capacity in comparison to the pure PAO. The results also show smaller variation in the specific heat capacity for pure PAO than the PAO-superstructure because of the nanoparticle and nanostructure presence.

An average of 44% enhancement was observed for the heat capacity ($2.37 kJ/kg°C$) with adding only 1% of each nanoparticle and PBP compared to pure PAO ($1.65 kJ/kg°C$) at 80°C. These experiments have been conducted with a total of six samples which have been separately synthesized and tested on different days. The standard error is $0.05 kJ/kg°C$. Moreover, the peak in figure 4-6 is vague which indicates that the in-situ formation of the superstructure has happened and was completed in the first thermal cycle.

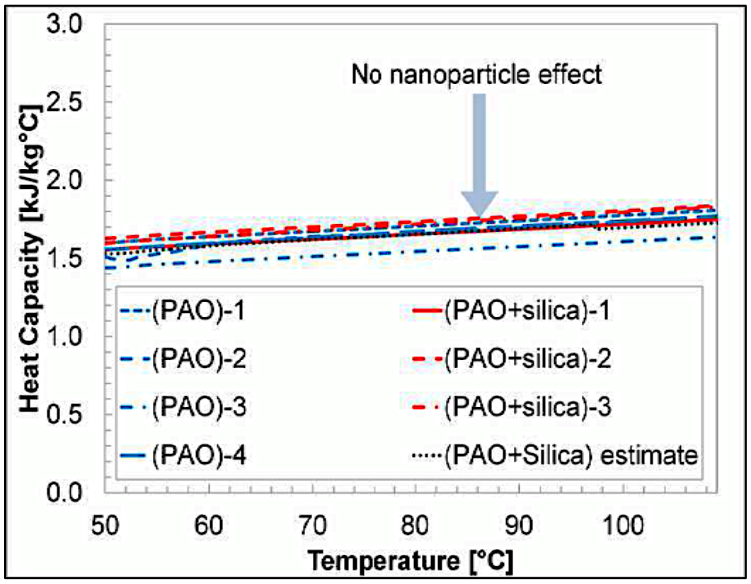


Figure 4-3 The DSC results for the specific heat capacity of pure PAO and PAO doped with $SiO_2$ nanoparticles (1 wt. %).

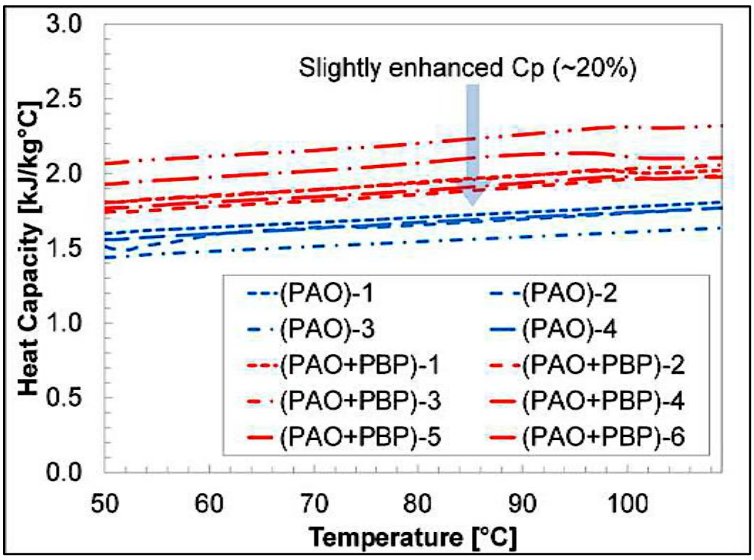


Figure 4-4 The DSC results for the specific heat capacity of pure PAO and its nanofluid (doped with proposed pre-fabricated nano-additives (i.e., polyethylene-block-poly (PBP)

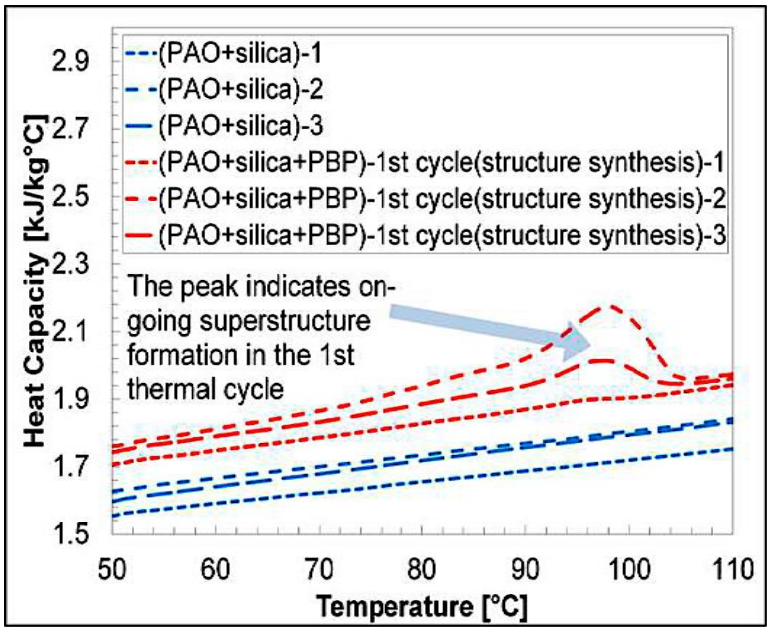


Figure 4-5 The initial DSC results of the proposed pre-fabricated nano-additives (i.e., polyethylene-block-poly (PBP)) together with $SiO_2$ nanoparticles in PAO.

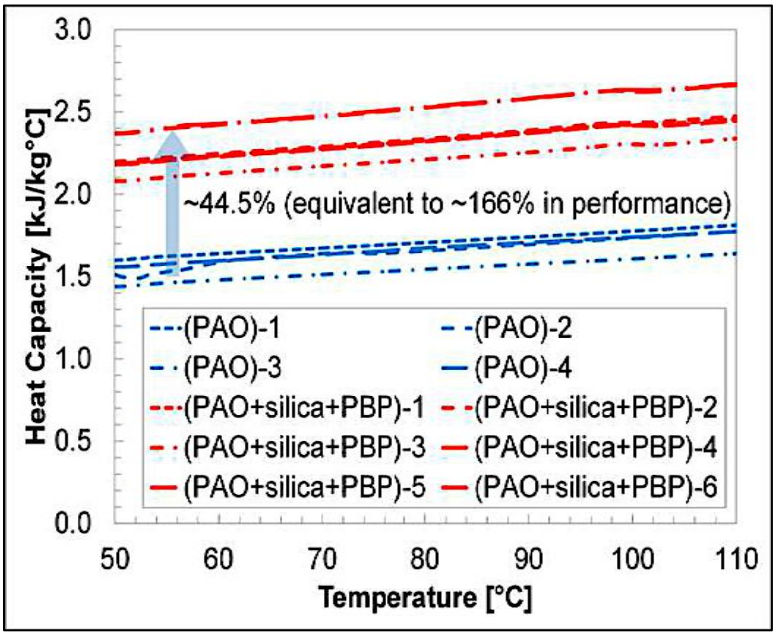


Figure 4-6 DSC results for specific heat capacity measurements of PAO + $SiO_2$ nanoparticles + PBP after the first thermal cycle.

Table 4-1 DSC results for specific heat capacity measurement at 80 °C.

| | Pure PAO | PAO+ 1% $SiO_2$ | PAO+ 1% PBP | PAO+ 1% $SiO_2$+ 1% PBP 1st cycle | PAO+ 1% $SiO_2$+ 1% PBP 2nd cycle |
|---|---|---|---|---|---|
| $C_p$ $(kJ/kg°C)$ First test | 1.71 | 1.66 | 1.93 | 1.83 | 2.33 |
| $C_p$ $(kJ/kg°C)$ Second test | 1.66 | 1.73 | 1.87 | 1.94 | 2.34 |
| $C_p$ $(kJ/kg°C)$ Third test | 1.54 | 1.72 | 1.95 | 1.89 | 2.21 |
| $C_p$ $(kJ/kg°C)$ Fourth test | 1.67 | - | 2.07 | - | 2.32 |
| $C_p$ $(kJ/kg°C)$ Fifth test | - | - | 1.89 | - | 2.52 |
| $C_p$ $(kJ/kg°C)$ Sixth test | - | - | 2.2 | - | 2.53 |
| Average $C_p$ $(kJ/kg°C)$ | 1.64 | 1.70 | 1.99 | 1.88 | 2.37 |
| Enhancement | - | 3.7% | 21.04% | 14.6% | 44.5% |
| Standard deviation | 0.07 | 0.04 | 0.12 | 0.06 | 0.06 |

The repeatability of the results has been presented in figure 4-7. The sample from the fifth and sixth test have been chosen from figure 4-6 and repeated three times for each sample. The result confirms that all the experiments have an excellent agreement and also shows that there was no significant specific heat capacity change. The standard error of experiments for each sample was only 0.002 $kJ/kg°C$.

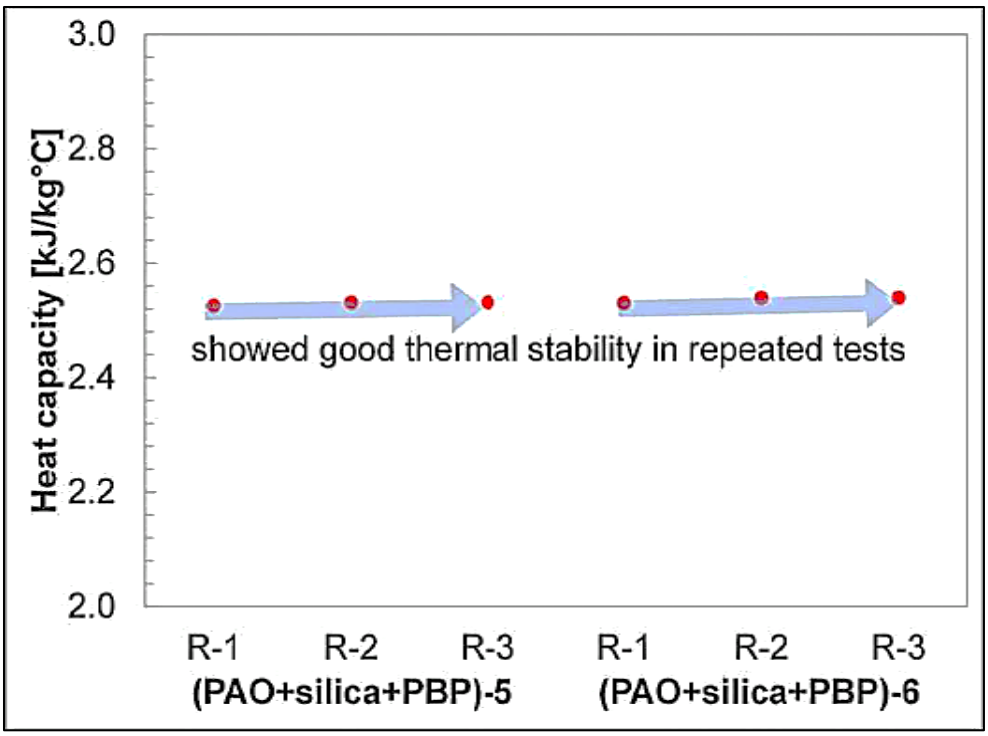


Figure 4-7 The DSC results for the specific heat capacity measurement of PAO + $SiO_2$ nanoparticles + PBP up to three repeats.

No significant degradation of specific heat capacity was observed.

### *4.2. Material characterization of PBP*

Polyethylene-block-poly (ethylene glycol) with a molecular weight of 1400 (know as medium chain PBP) was taken to a scanning electron microscope (SEM S-300N) for material characterization. SEM images with different magnifications were taken. Unfortunately, the images were vague, and after 1k magnification nothing was visible. The PBP is a very highly charged material that SEM S-300N, even in a low vacuum, could not give us an image from the sample. Therefore the S-4800 HRSEM was used for further material characterization.

#### *4.2.1. The ground PBP vs. PBP*

To make the PAO nanofluid, the PBP was ground manually, to have a homogeneous nanofluid. The ground PBP and PBP have been coated with Ag gas in a CRC – 100 Sputtering system coating machine (plasma science, Inc), before taking it to HRSEM. However, coating had a reverse effect and prevented us from seeing an image for PBP.

In the next attempt, the sample was used in the HRSEM without any coatings. Fortunately, with HRSEM we could go to a very low vacuum and see some images to help us identify the difference between ground PBP and PBP. However, after a specific magnification, the PBP charge prevented us from taking a more profound image. PBP below 20K magnification and ground PBP below 10k were the only allowable magnified option. With these magnifications, it is not possible to observe PBP, and any impression from the taken images could not be used to evaluate PBP characteristics, and the highly charged PBP prevented the HRSEM from giving us an image in the nominal size range of the PBP.

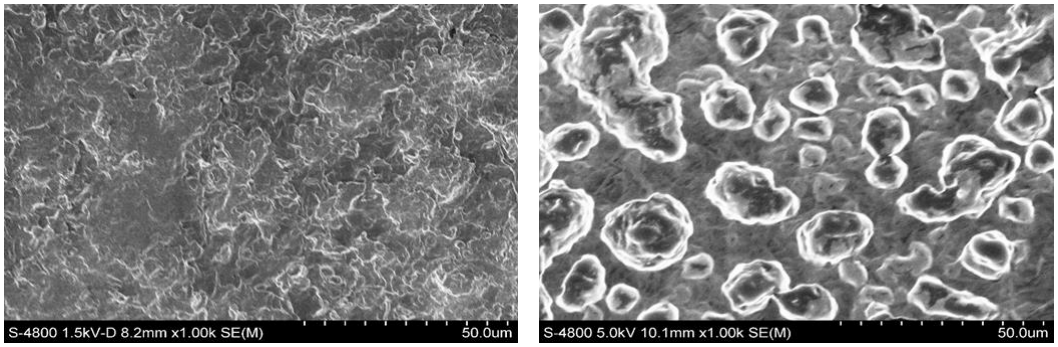


Figure 4-8 PBP (left) vs. Ground PBP (right) at 1K magnification

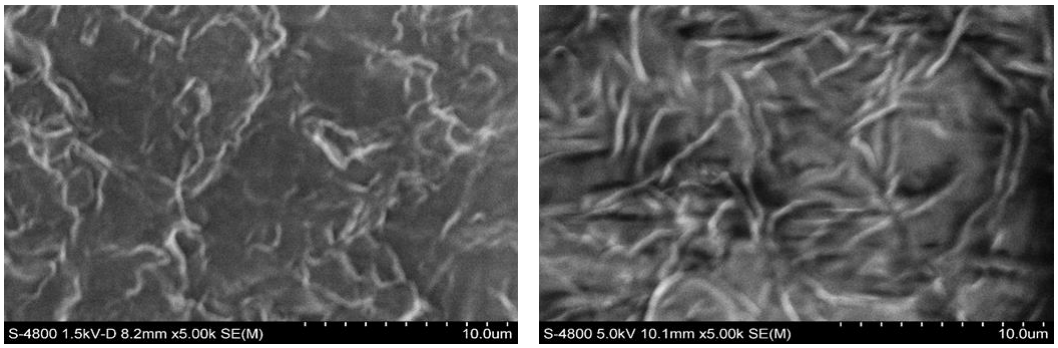


Figure 4-9 PBP (left) vs. Ground PBP (right) at 5K magnification

The Differential Scanning Calorimetry (DSC) measurements have been done for ground PBP and PBP. Figure 4-10 through 4-12, and figures 4-13 through 4-15 show the specific heat capacity results of the PBP, and ground PBP, respectively (3 different tests to confirm the reliability of the results). Table 4-2 to 4-4 summarize the DSC result in 80℃ for better comparison. The ground PBP has an average of 17.6% enhancement in specific heat capacity for the first cycle and 18.4% and 14.8% enhancement for second and third cycles respectively.

As you see below, the first cycle of every sample is lower than the second and third, which is because of the irregularity of sample materials when they are first loaded. Since samples are not uniform when they are loaded in the power form, heat flow into the

sample may not be homogeneous, and thus the specific heat capacity result does not agree with the second and third cycle. On the other hand, once each sample melts in their first cycle, they may be settling down homogenously, and as a result, the heat flow inside the DSC can be more reliable (Hence, the second and third cycle data agree with each other).

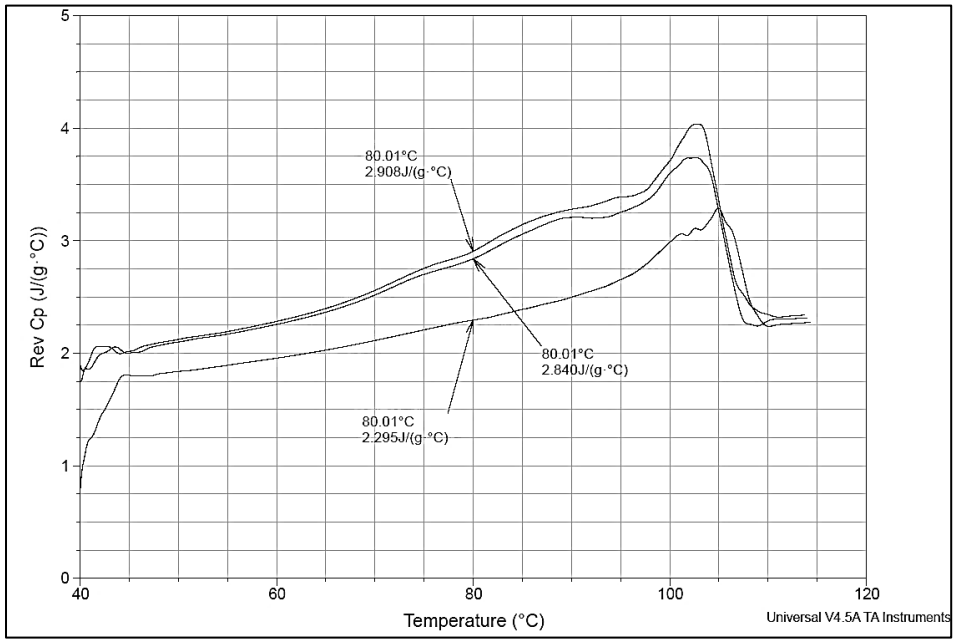


Figure 4-10 DSC measurement of PBP #1

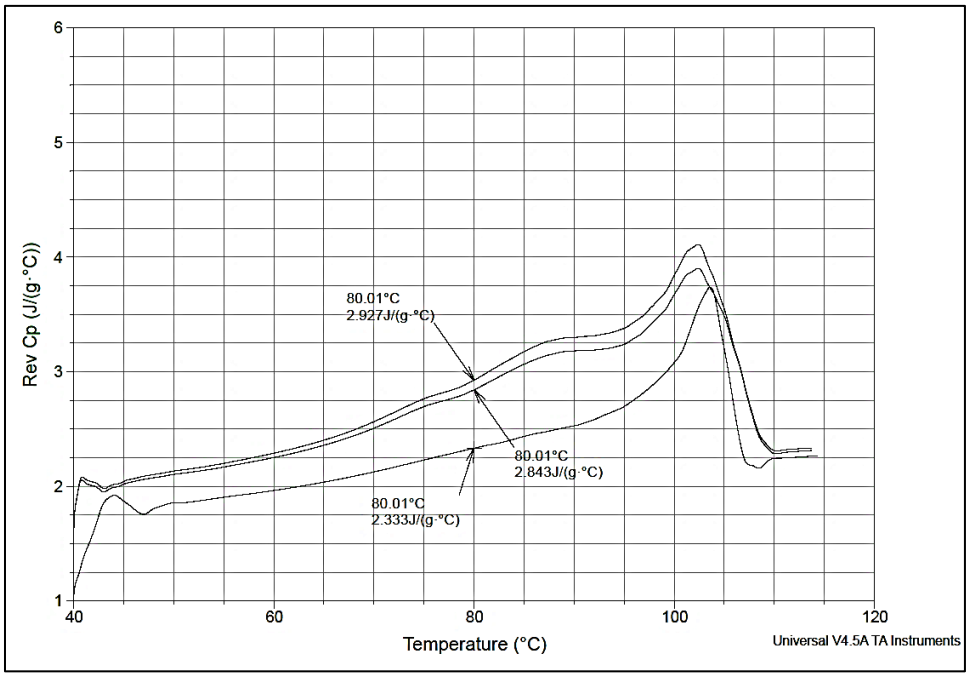


Figure 4-11 DSC measurement of PBP #2

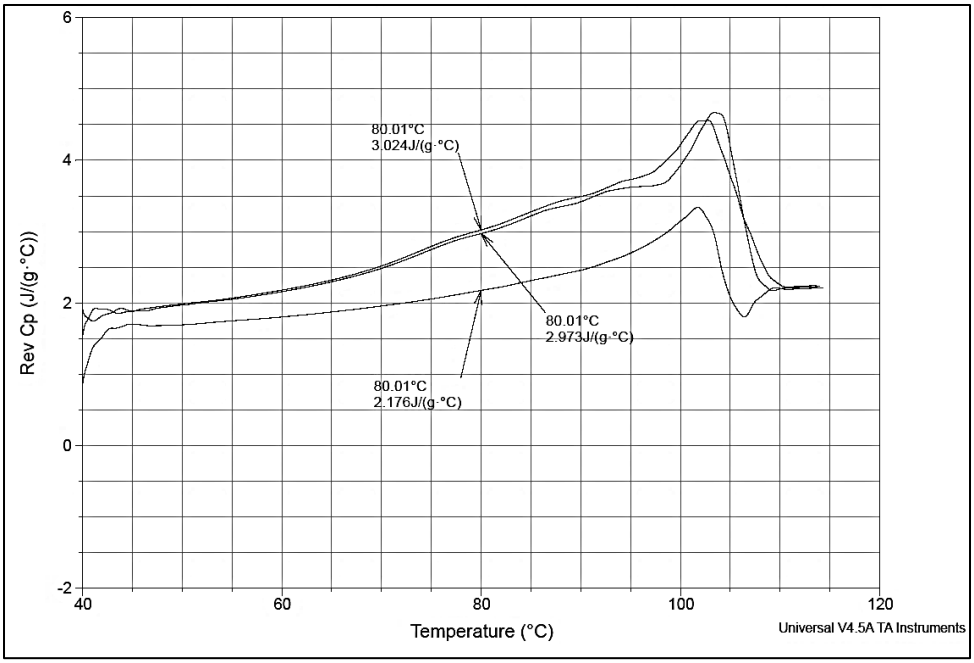


Figure 4-12 DSC measurement of PBP #3

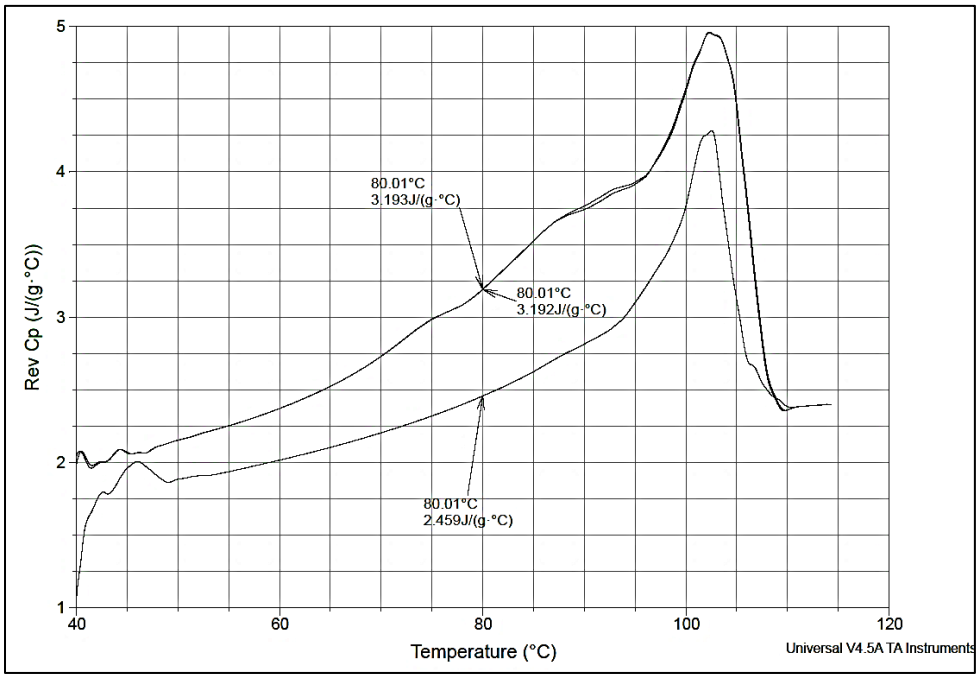


Figure 4-13 DSC measurement of ground PBP #1

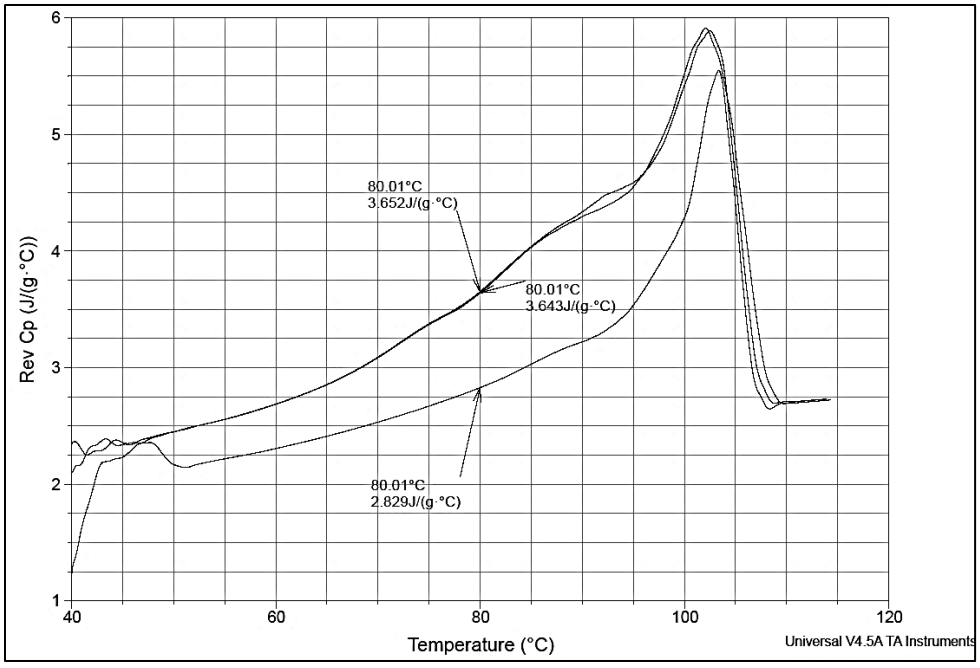


Figure 4-14 DSC measurement of ground PBP #2

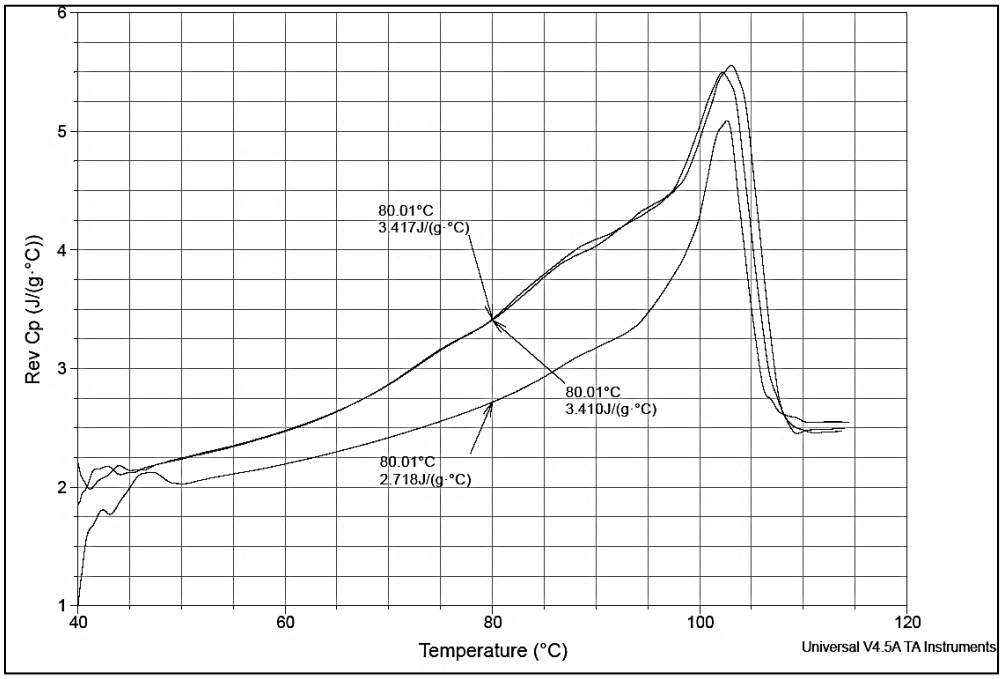


Figure 4-15 DSC measurement of ground PBP #3

Table 4-2 A summary of Specific heat capacity measurement of PBP at 80 °C

| | PBP#1 | PBP#2 | PBP#3 | Average | Standard deviation |
|---|---|---|---|---|---|
| $C_p\ (kJ/kg°C)$ First cycle | 2.3 | 2.33 | 2.18 | 2.27 | 0.07 |
| $C_p\ (kJ/kg°C)$ Second cycle | 2.84 | 2.84 | 2.97 | 2.88 | 0.07 |
| $C_p\ (kJ/kg°C)$ Third cycle | 2.91 | 2.93 | 3.1 | 2.98 | 0.1 |

Table 4-3 A summary of specific heat capacity measurement of ground PBP at 80 °C

| | Ground PBP#1 | Ground PBP#2 | Ground PBP#3 | Average | Standard deviation |
|---|---|---|---|---|---|
| $C_p\ (kJ/kg°C)$ First cycle | 2.46 | 2.83 | 2.72 | 2.67 | 0.1 |
| $C_p\ (kJ/kg°C)$ Second cycle | 3.192 | 3.64 | 3.41 | 3.414 | 0.2 |
| $C_p\ (kJ/kg°C)$ Third cycle | 3.193 | 3.65 | 3.42 | 3.421 | 0.2 |

Table 4-4 A comparison between the specific heat capacity of PBP vs. ground PBP

| | PBP | Ground PBP | enhancement |
|---|---|---|---|
| Average $C_p\ (kJ/kg°C)$ First cycle | 2.27 | 2.67 | 17.6 % |
| Average $C_p\ (kJ/kg°C)$ Second cycle | 2.88 | 3.414 | 18.4% |
| Average $C_p\ (kJ/kg°C)$ Third cycle | 2.98 | 3.421 | 14.8% |

### *4.3. Thermal conductivity*

The thermal conductivity experiments for Pure PAO were repeated in three separate experiments to get a valid reference value, and the average value calculated to be 0.138 $W/m°C$. The PAO + $SiO_2$ nanoparticles (1 wt. %) + PBP (1 wt. %) were also tested 3 times to make sure of the repeatability of the results. Results are presented in table 4-5 and figure 4-16.

All the thermal conductivity experiments were conducted at a constant temperature of 120°C. The results show an average thermal conductivity enhancement of 19.8%.

Mechanisms responsible for increased thermal conductivity are [79], 1) Brownian motion, 2) clustering of nanoparticles, 3) liquid layering around nanoparticles, 4) ballistic phonon transport in nanoparticles, 5) near field radiation.

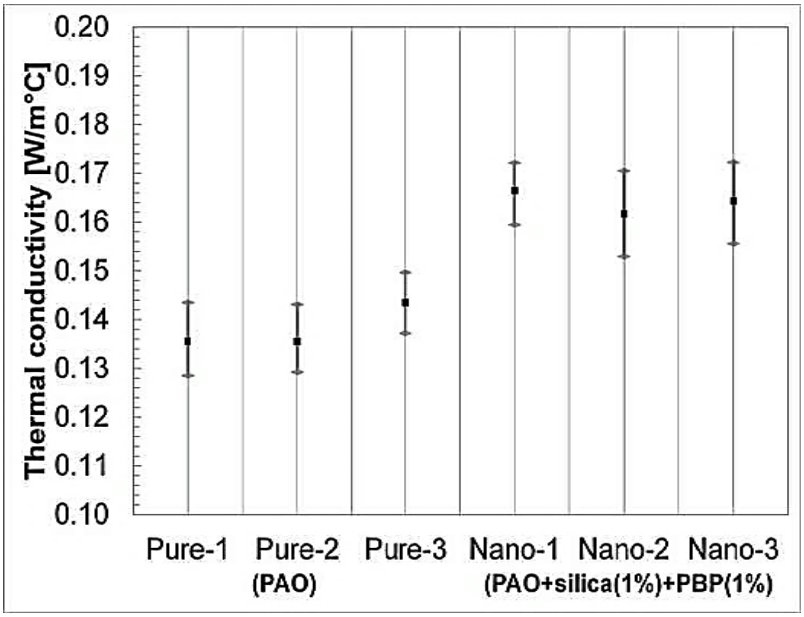


Figure 4-16 the results of the conductivity measurements of pure PAO and PAO-superstructure ($SiO_2$ (1 wt. %) + PBP (1 wt. %))

Table 4-5 Thermal conductivity measurement at 120°C

| | Pure PAO | PAO+ 1% $SiO_2$ + 1% PBP |
|---|---|---|
| $K\ (W/m°C)$ First test | 0.137 | 0.167 |
| $K\ (W/m°C)$ Second test | 0.136 | 0.164 |
| $K\ (W/m°C)$ Third test | 0.142 | 0.165 |
| Average $K\ (W/m°C)$ | 0.138 | 0.165 |
| Enhancement (%) | - | 19.8% |
| Standard deviation | 0.003 | 0.001 |

### *4.4. Viscosity*

First, the rheometer was used to conduct the experiments for pure PAO. The constant temperature of 120°C was set. Figure 4-17 and table 4-6 present the three repeated results of Pure PAO with the shear rate from 100 /s to 1000 /s.

The viscosity of pure PAO was detected to be independent of shear rate, and therefore it has the Newtonian behavior. In contrary the viscosity of $PAO + SiO_2\ (1\%) + PBP\ (1\%)$ was observed to decrease with the shear rate increase. Such shear thining is as a result of the nanoparticles presence together with PBP bonded to the nanoparticles (existing of the superstructure, that also has a high aspect ratio). The average viscosity enhancement is from 18% at the shear rate of 1000 /s to 29% at the shear rate of 200 /s, compared to pure PAO, (Table 4-6).

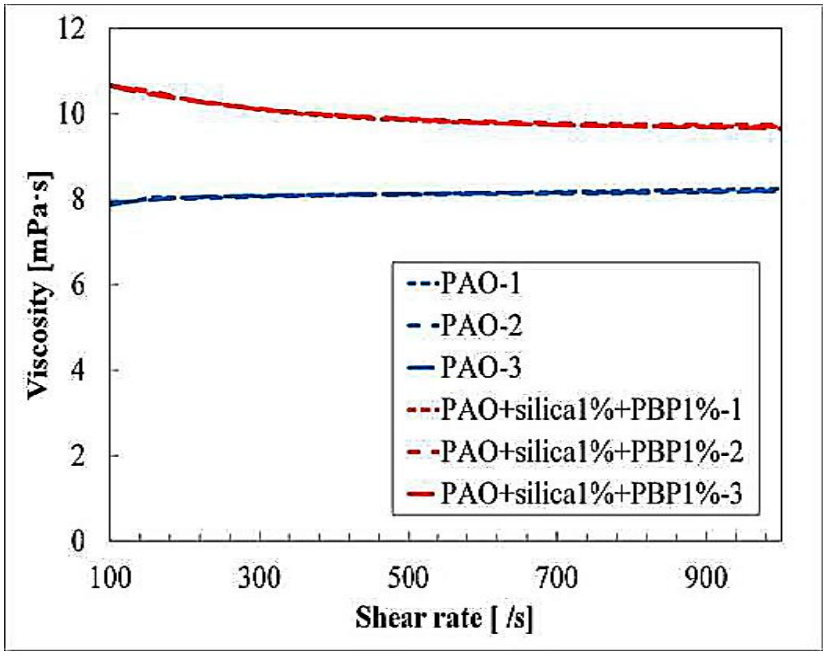


Figure 4-17 The results of the viscosity measurements of Pure PAO and PAO-superstructure ($SiO_2$ (1wt. %) + PBP (1wt. %)).

Table 4-6 Results of the viscosity measurements at 120°C

| shear rate ( $1/s$ ) | Pure PAO First test ($mPa.s$) | Pure PAO Second test ($mPa.s$) | Pure PAO Third test ($mPa.s$) | PAO+ 1% $SiO_2$ + 1% PBP First test ($mPa.s$) | PAO+ 1% $SiO_2$ + 1% PBP Second test ($mPa.s$) | PAO+ 1% $SiO_2$ + 1% PBP Third test ($mPa.s$) |
|---|---|---|---|---|---|---|
| 100 | 7.91 | 7.87 | 7.92 | 10.67 | 10.66 | 10.66 |
| 126 | 7.94 | 7.94 | 7.94 | 10.59 | 10.60 | 10.55 |
| 158 | 8.04 | 8.01 | 7.99 | 10.48 | 10.52 | 10.45 |
| 200 | 8.04 | 8.01 | 8.04 | 10.35 | 10.36 | 10.33 |
| 251 | 8.06 | 8.04 | 8.07 | 10.22 | 10.22 | 10.20 |
| 316 | 8.08 | 8.06 | 8.09 | 10.07 | 10.09 | 10.08 |
| 398 | 8.10 | 8.09 | 8.11 | 9.94 | 9.98 | 9.97 |
| 501 | 8.12 | 8.11 | 8.13 | 9.84 | 9.89 | 9.87 |
| 631 | 8.15 | 8.12 | 8.15 | 9.77 | 9.81 | 9.77 |
| 794 | 8.19 | 8.14 | 8.16 | 9.71 | 9.76 | 9.71 |
| 1000 | 8.24 | 8.19 | 8.20 | 9.67 | 9.71 | 9.63 |

### *4.5. The figure of merit analysis*

The enhancements in thermal conductivity and specific heat capacity can advance the PAO's heat transfer and storage performance. Conversely, the enhancement of the viscosity may have negative effect on the pumping power and rise the pumping power. Hence, it is essential to analyze the effect of the proposed in-situ synthesis of the PAO superstructure to see whether it is beneficial in advanced heat transfer fluid applications.

For heat storage performance, Bonilla [80] presented a figure of merit to define the performance of a specified storage fluid in comparison to its required pumping power to preserve temperature difference between the outlet and inlet of the storage fluid for forced convection in the turbulent regime:

$$FOM_1 = \frac{\rho^{2.0} {C_p}^{2.8}}{\mu^{0.2}} \tag{22}$$

For heat transfer performance, Lenert [81] improved mouromtseff number to take effect on the conductive heat transfer coefficient (the radial direction) in consideration, and also combine the effect of the thermal storage capacity (axial direction) in a turbulent flow:

$$FOM_2 = \frac{\rho^{2.0} {C_p}^{1.6} K^{1.8}}{\mu^{1.4}} \tag{23}$$

Assuming the constant density; results of $FOM_1$ and $FOM_2$ analyses are presented in table 4-7.

The average value of the specific heat capacity enhancement (44.5%) and the average value of the thermal conductivity enhancement (19.8%) are substituted to Equations 22 and 23. As shown in figure 4-19 and table 4-5 the viscosity of PAO-superstructure has a non-Newtonian (shear thinning) behavior, so the minimum enhancement of 18% at the shear rate of 1000 /s and the maximum enhancement of 29% at the shear rate of 100 /s are used to calculate $FOM_1$ and $FOM_2$. Results confirmed that the performance of PAO for heat storage can be increased by ~166-171% and also for heat transfer by ~75-98%.

Table 4-7 Figure of merit analyses ($FOM_1$ and $FOM_2$)

| Properties & Figure of Merit | Effect of superstructure ($SiO_2$ +PBP) doped into PAO |
|---|---|
| $C_p$ % | 44.5 |
| $K$ % | 19.8 |
| $\mu$ % | 18~29 (from 100 /s to 1000 /s) |
| $FOM_1$ (heat storage performance) % | 2.66 - 2.71 |
| $FOM_2$ (heat transfer performance) % | 1.75 - 1.98 |

# Chapter 5

## Conclusion

In this study, the specific heat capacity of molten salt nano-eutectic ($Li_2CO_3 - K_2CO_3$ doped with $SiO_2$ nanoparticles) was theoretically investigated. According to the proposed theory in the literature [3], the effective specific heat capacity of a nano-eutectic can be significantly enhanced by the formation of needle-like nanostructures by salt eutectic. The specific heat capacity model (equation 1) was modified by adding the nanostructure parameters, its specific heat capacity and mass fraction. To investigate the effect of the formed nanostructure, its specific heat capacity was theoretically calculated by expanding the model used by Wang and other researchers [2], [66], [67] The mass fraction of the formed nanostructure was estimated by MATLAB using the reported material characterization study [3]. The binary carbonate with different size of doped nanoparticle selected to test the nanostructure theory along with our modified formula. The theoretical predictions from Equation 2 was in a good agreement with the measured specific heat capacity values from the literature [3] with an error less than 4%. The result shows that the enhanced specific heat capacity of a nano-eutectic can be explained by the contribution of the formed nanostructure, and the mass fraction of the nanostructure is wholly dependent to the nanoparticle size and varies along with different diameters of the doped nanoparticle. The present approach was only applied to a particular molten salt nano-eutectic ($Li_2CO_3 - K_2CO_3$) doped with $SiO_2$ nanoparticles) and needs to be tested for other types of nano-eutectics.

Moreover, to conclude the second study, the enhancement of specific heat capacity of molten salt nanofluid is because of a unique characteristic of the molten salt eutectic; the salt molecules are expected to have an electrostatic interaction with oxide nanoparticles and grow like a needle shape as they settle down on the nanoparticle surfaces to form the nanostructure. Thus, such formation of nanostructures appears to happen only in molten salt nanofluids and because such specific heat capacity enhancement of the base fluid only naturally occurs in

molten salts. In this research, we established that such nanostructures can be mimicked through the in-situ formation of the fabricated superstructure, created by nanoparticles coated with pre-fabricated nanostructures which we call superstructure, (i.e., hydroxy-ended poly (Polyethylene-Block-Poly) [MW ca. 1,400], termed as “PBP”). We first utilized this method to polyalphaolefin (PAO), a well-known non-polar oil for advanced heat transfer fluid applications such as the aviation platform in military applications and as a coolant in the radar systems. A differential scanning calorimeter (DSC) was conducted to run the experiments and to characterize the specific heat capacity.

Meanwhile, these formed structures can also enhance the thermal conductivity and viscosity of the nanofluids. Enhancement of 44.5%, 19.8% and 22.5% for the specific heat capacity, thermal conductivity, and viscosity of the nanofluid was observed, respectively. DSC material characterization was conducted to see the effect of grinding on PBP and was observed that it would increase the specific heat capacity of the PBP by 17.6%, 18.4%, and 14.8% for first, second, and third thermal cycle, respectively.

Furthermore, the specific heat capacity and thermal conductivity enhancements can advance PAO’s heat transfer and storage performances. Conversely, the enhanced viscosity may increase the pumping power (a very negative effect). Therefore it is essential to estimate the effect of the proposed in-situ synthesis of the superstructure in PAO to determine whether it is beneficial in advanced heat transfer fluid applications. Therefore, we estimated its heat transfer and storage performance by analyzing the general figure of merit. Results show that heat transfer and storage performances can be increased by ~166-177% and ~75-98%, respectively. This research is the first demonstration of enhanced specific heat capacity by in-situ formation of the nanostructures and offers a new approach to organic molecule-modification to the materials science community.

References

[1] M. Lasfargues, A. Bell, and Y. Ding, “In situ production of titanium dioxide nanoparticles in molten salt phase for thermal energy storage and heat-transfer fluid applications,” *J. Nanoparticle Res.*, vol. 18, no. 6, pp. 1–11, 2016.

[2] B.-X. Wang, L.-P. Zhou, and X.-F. Peng, “Surface and Size Effects on the Specific Heat Capacity of Nanoparticles,” *Int. J. Thermophys.*, vol. 27, no. 1, pp. 139–151, 2006.

[3] H. Tiznobaik and D. Shin, “Enhanced specific heat capacity of high-temperature molten salt-based nanofluids,” *Int. J. Heat Mass Transf.*, vol. 57, no. 2, pp. 542–548, 2013.

[4] S. U. S. Choi and J. A. Eastman, “Enhancing thermal conductivity of fluids with nanoparticles,” *ASME Int. Mech. Eng. Congr. Expo.*, vol. 66, no. March, pp. 99–105, 1995.

[5] K. V. Wong and O. De Leon, “Applications of nanofluids: Current and future,” *Adv. Mech. Eng.*, vol. 2010, 2010.

[6] P. Keblinski, J. A. Eastman, and D. G. Cahill, “Nanofluids for thermal transport,” *Mater. Today*, vol. 8, no. 6, pp. 36–44, 2005.

[7] X. Q. Wang and A. S. Mujumdar, “Heat transfer characteristics of nanofluids: a review,” *Int. J. Therm. Sci.*, vol. 46, no. 1, pp. 1–19, 2007.

[8] J. A. Eastman, S. U. S. Choi, S. Li, W. Yu, and L. J. Thompson, “Anomalously increased effective thermal conductivities of ethylene glycol-based nanofluids containing copper nanoparticles,” *Appl. Phys. Lett.*, vol. 78, no. 6, pp. 718–720, 2001.

[9] J. Eapen, W. C. Williams, J. Buongiorno, L. W. Hu, S. Yip, R. Rusconi, and R. Piazza, “Mean-field versus microconvection effects in nanofluid thermal conduction,” *Phys. Rev. Lett.*, vol. 99, no. 9, pp. 1–4, 2007.

[10] S. K. Das, N. Putra, P. Thiesen, and W. Roetzel, “Temperature Dependence of Thermal Conductivity Enhancement for Nanofluids,” *J. Heat Transfer*, vol. 125, no. 4, p. 567, 2003.

[11] C. H. Li and G. P. Peterson, “Experimental investigation of temperature and volume fraction variations on the effective thermal conductivity of nanoparticle suspensions (nanofluids),” *J. Appl. Phys.*, vol. 99, no. 8, 2006.

[12] P. K, “M echanisms of heat ¯ ow in suspensions of nano-sized particles nano ¯ uids ),” vol. 45, pp. 855–863, 2002.

[13] S. P. Jang and S. U. S. Choi, “Role of Brownian motion in the enhanced thermal conductivity of nanofluids,” *Appl. Phys. Lett.*, vol. 84, no. 21, pp. 4316–4318, 2004.

[14] W. Evans, J. Fish, and P. Keblinski, “Role of Brownian motion hydrodynamics on nanofluid thermal conductivity,” *Appl. Phys. Lett.*, vol. 88, no. 9, 2006.

[15] W. Yu and S. U. S. Choi, “The role of interfacial layers in the enhanced thermal conductivity of nanofluids: A renovated Maxwell model,” *J. Nanoparticle Res.*, vol. 5, no. 1–2, pp. 167–171, 2003.

[16] L. Xue, P. Keblinski, S. R. Phillpot, S. U. S. Choi, and J. A. Eastman, “Effect of liquid layering at the liquid-solid interface on thermal transport,” *Int. J. Heat Mass Transf.*, vol. 47, no. 19–20, pp. 4277–4284, 2004.

[17] R. Prasher, P. E. Phelan, and P. Bhattacharya, “Effect of aggregation kinetics on the thermal conductivity of nanoscale colloidal solutions (nanofluid),” *Nano Lett.*, vol. 6, no. 7, pp. 1529–1534, 2006.

[18] P. Keblinski, R. Prasher, and J. Eapen, “Thermal conductance of nanofluids: Is the controversy over?,” *J. Nanoparticle Res.*, vol. 10, no. 7, pp. 1089–1097, 2008.

[19] J. Buongiorno, D. C. Venerus, N. Prabhat, T. McKrell, J. Townsend, R. Christianson, Y. V. Tolmachev, P. Keblinski, L. W. Hu, J. L. Alvarado, I. C. Bang, S. W. Bishnoi, M. Bonetti, F. Botz, A. Cecere, Y. Chang, G. Chen, H. Chen, S. J. Chung, M. K. Chyu, S. K. Das, R. Di Paola, Y. Ding, F. Dubois, G. Dzido, J. Eapen, W. Escher, D. Funfschilling, Q. Galand, J. Gao, P. E. Gharagozloo, K. E. Goodson, J. G. Gutierrez, H. Hong, M. Horton, K. S. Hwang, C. S. Iorio, S. P. Jang, A. B. Jarzebski, Y. Jiang, L. Jin, S. Kabelac, A.

Kamath, M. A. Kedzierski, L. G. Kieng, C. Kim, J. H. Kim, S. Kim, S. H. Lee, K. C. Leong, I. Manna, B. Michel, R. Ni, H. E. Patel, J. Philip, D. Poulikakos, C. Reynaud, R. Savino, P. K. Singh, P. Song, T. Sundararajan, E. Timofeeva, T. Tritcak, A. N. Turanov, S. Van Vaerenbergh, D. Wen, S. Witharana, C. Yang, W. H. Yeh, X. Z. Zhao, and S. Q. Zhou, “A benchmark study on the thermal conductivity of nanofluids,” *J. Appl. Phys.*, vol. 106, no. 9, 2009.

[20] J. H. Lee, K. S. Hwang, S. P. Jang, B. H. Lee, J. H. Kim, S. U. S. Choi, and C. J. Choi, “Effective viscosities and thermal conductivities of aqueous nanofluids containing low volume concentrations of Al2O3nanoparticles,” *Int. J. Heat Mass Transf.*, vol. 51, no. 11–12, pp. 2651–2656, 2008.

[21] H. Xie, J. Wang, T. Xi, and Y. Liu, “Thermal Conductivity of Suspensions Containing Nanosized SiC Particles,” *Int. J. Thermophys.*, vol. 23, no. 2, pp. 571–580, 2002.

[22] T.-K. Hong, H.-S. Yang, and C. J. Choi, “Study of the enhanced thermal conductivity of Fe nanofluids,” *J. Appl. Phys.*, vol. 97, no. 6, p. 064311, 2005.

[23] M. J. Assael, C. F. Chen, I. Metaxa, and W. A. Wakeham, “Thermal conductivity of suspensions of carbon nanotubes in water,” *Int. J. Thermophys.*, vol. 25, no. 4, pp. 971–985, 2004.

[24] R. Prasher, D. Song, J. Wang, and P. Phelan, “Measurements of nanofluid viscosity and its implications for thermal applications,” *Appl. Phys. Lett.*, vol. 89, no. 13, pp. 1–4, 2006.

[25] H. Chen, Y. Ding, and C. Tan, “Rheological behaviour of nanofluids,” *New J. Phys.*, vol. 9, 2007.

[26] M. Chandrasekar, S. Suresh, and A. Chandra Bose, “Experimental investigations and theoretical determination of thermal conductivity and viscosity of Al2O3/water nanofluid,” *Exp. Therm. Fluid Sci.*, vol. 34, no. 2, pp. 210–216, 2010.

[27] C. T. Nguyen, F. Desgranges, G. Roy, N. Galanis, T. Maré, S. Boucher, and H. Angue Mintsa, “Temperature and particle-size dependent viscosity data for water-based

nanofluids - Hysteresis phenomenon," *Int. J. Heat Fluid Flow*, vol. 28, no. 6, pp. 1492–1506, 2007.

[28] Y. He, Y. Jin, H. Chen, Y. Ding, D. Cang, and H. Lu, "Heat transfer and flow behaviour of aqueous suspensions of TiO2nanoparticles (nanofluids) flowing upward through a vertical pipe," *Int. J. Heat Mass Transf.*, vol. 50, no. 11–12, pp. 2272–2281, 2007.

[29] D. Numburu, P; Kulkarni, D; Dandekar, A; Das, "Experimental investigation of viscosity and specific heat of silicon dioxide nanofluids," *Micro Nano Lett.*, vol. 2, no. 3, pp. 67–71, 2007.

[30] S.-Q. Zhou and R. Ni, "Measurement of the specific heat capacity of water-based Al2O3 nanofluid," *Appl. Phys. Lett.*, vol. 92, no. 9, p. 093123, 2008.

[31] R. S. Vajjha and D. K. Das, "Specific Heat Measurement of Three Nanofluids and Development of New Correlations," *J. Heat Transfer*, vol. 131, no. 7, p. 071601, 2009.

[32] J. Buongiorno, "Convective Transport in Nanofluids," *J. Heat Transfer*, vol. 128, no. 3, p. 240, 2006.

[33] D. Shin and D. Banerjee, "Enhanced Specific Heat of Silica Nanofluid," *J. Heat Transfer*, vol. 133, no. 2, p. 024501, 2011.

[34] D. Shin and D. Banerjee, "Enhancement of specific heat capacity of high-temperature silica-nanofluids synthesized in alkali chloride salt eutectics for solar thermal-energy storage applications," *Int. J. Heat Mass Transf.*, vol. 54, no. 5–6, pp. 1064–1070, 2011.

[35] M. X. Ho and C. Pan, "Optimal concentration of alumina nanoparticles in molten hitec salt to maximize its specific heat capacity," *Int. J. Heat Mass Transf.*, vol. 70, pp. 174–184, 2014.

[36] M. Schuller, Q. Shao, and T. Lalk, "Experimental investigation of the specific heat of a nitrate-alumina nanofluid for solar thermal energy storage systems," *Int. J. Therm. Sci.*, vol. 91, pp. 142–145, 2015.

[37] G. Qiao, M. Lasfargues, A. Alexiadis, and Y. Ding, "Simulation and experimental study of

the specific heat capacity of molten salt based nanofluids," *Appl. Therm. Eng.*, vol. 111, pp. 1517–1522, 2017.

[38] B. Dudda and D. Shin, "Effect of nanoparticle dispersion on specific heat capacity of a binary nitrate salt eutectic for concentrated solar power applications," *Int. J. Therm. Sci.*, vol. 69, pp. 37–42, 2013.

[39] D. Seo, Joohyun;Shin, "Enhancement of specific heat of ternary nitrate (LiNO3-NaNO3-KNO3) salt by doping with SiO2 nanoparticles for solar thermal energy storage," *Micro Nano Lett.*, vol. 9, no. 11, pp. 817–820, 2014.

[40] D. Shin and D. Banerjee, "Specific heat of nanofluids synthesized by dispersing alumina nanoparticles in alkali salt eutectic," *Int. J. Heat Mass Transf.*, vol. 74, pp. 210–214, 2014.

[41] H. Tiznobaik, D. Banerjee, and D. Shin, "Effect of formation of 'long range' secondary dendritic nanostructures in molten salt nanofluids on the values of specific heat capacity," *Int. J. Heat Mass Transf.*, vol. 91, pp. 342–346, 2015.

[42] J. Seo and D. Shin, "Size effect of nanoparticle on specific heat in a ternary nitrate (LiNO3-NaNO3-KNO3) salt eutectic for thermal energy storage," *Appl. Therm. Eng.*, vol. 102, pp. 144–148, 2016.

[43] M. Chieruzzi, G. F. Cerritelli, A. Miliozzi, and J. M. Kenny, "Effect of nanoparticles on heat capacity of nanofluids based on molten salts as PCM for thermal energy storage," *Nanoscale Res. Lett.*, vol. 8, no. 1, pp. 1–9, 2013.

[44] P. Andreu-cabedo, R. Mondragon, L. Hernandez, R. Martinez-cuenca, L. Cabedo, and J. E. Julia, "Increment of specific heat capacity of solar salt with SiO 2 nanoparticles," *Nanoscale Res. Lett.*, vol. 9, p. 582, 2014.

[45] H. Tiznobaik and D. Shin, "Experimental validation of enhanced heat capacity of ionic liquid-based nanomaterial," *Appl. Phys. Lett.*, vol. 102, no. 17, pp. 2011–2014, 2013.

[46] D. Shin and D. Banerjee, "Enhanced Specific Heat Capacity of Nanomaterials

Synthesized by Dispersing Silica Nanoparticles in Eutectic Mixtures," *J. Heat Transfer*, vol. 135, no. 3, p. 032801, 2013.

[47] B. Jo and D. Banerjee, "Enhanced specific heat capacity of molten salt-based nanomaterials: Effects of nanoparticle dispersion and solvent material," *Acta Mater.*, vol. 75, pp. 80–91, 2014.

[48] Z. Zhang, Y. Yuan, L. Ouyang, Q. Sun, X. Cao, and S. Alelyani, "Enhanced thermal properties of Li2CO3–Na2CO3–K2CO3 nanofluids with nanoalumina for heat transfer in high-temperature CSP systems," *J. Therm. Anal. Calorim.*, vol. 128, no. 3, pp. 1783–1792, 2017.

[49] M. Chieruzzi, G. F. Cerritelli, A. Miliozzi, J. M. Kenny, and L. Torre, "Heat capacity of nanofluids for solar energy storage produced by dispersing oxide nanoparticles in nitrate salt mixture directly at high temperature," *Sol. Energy Mater. Sol. Cells*, vol. 167, no. March, pp. 60–69, 2017.

[50] Y. Hu, Y. He, Z. Zhang, and D. Wen, "Effect of Al2O3nanoparticle dispersion on the specific heat capacity of a eutectic binary nitrate salt for solar power applications," *Energy Convers. Manag.*, vol. 142, pp. 366–373, 2017.

[51] Y. Luo, X. Du, A. Awad, and D. Wen, "Thermal energy storage enhancement of a binary molten salt via in-situ produced nanoparticles," *Int. J. Heat Mass Transf.*, vol. 104, pp. 658–664, 2017.

[52] H. Riazi, S. Mesgari, N. A. Ahmed, and R. A. Taylor, "The effect of nanoparticle morphology on the specific heat of nanosalts," *Int. J. Heat Mass Transf.*, vol. 94, pp. 254–261, 2016.

[53] R. Devaradjane and D. Shin, "Nanoparticle Dispersions on Ternary Nitrate Salts for Heat Transfer Fluid Applications in Solar Thermal Power," *J. Heat Transfer*, vol. 138, no. 5, p. 051901, 2016.

[54] M. X. Ho and C. Pan, "Experimental investigation of heat transfer performance of molten

HITEC salt flow with alumina nanoparticles," *Int. J. Heat Mass Transf.*, vol. 107, pp. 1094–1103, 2017.

[55] L. di Zhang, X. Chen, Y. ting Wu, Y. wei Lu, and C. fang Ma, "Effect of nanoparticle dispersion on enhancing the specific heat capacity of quaternary nitrate for solar thermal energy storage application," *Sol. Energy Mater. Sol. Cells*, vol. 157, pp. 808–813, 2016.

[56] J. Navas, A. Sánchez-Coronilla, E. I. Martín, M. Teruel, J. J. Gallardo, T. Aguilar, R. Gómez-Villarejo, R. Alcántara, C. Fernández-Lorenzo, J. C. Piñero, and J. Martín-Calleja, "On the enhancement of heat transfer fluid for concentrating solar power using Cu and Ni nanofluids: An experimental and molecular dynamics study," *Nano Energy*, vol. 27, pp. 213–224, 2016.

[57] H. Tian, W. Wang, J. Ding, X. Wei, and C. Huang, "Preparation of binary eutectic chloride/expanded graphite as high-temperature thermal energy storage materials," *Sol. Energy Mater. Sol. Cells*, vol. 149, pp. 187–194, 2016.

[58] D. Shin, H. Tiznobaik, and D. Banerjee, "Specific heat mechanism of molten salt nanofluids," *Appl. Phys. Lett.*, vol. 104, no. 12, 2014.

[59] E. Parthé and L. M. Gelato, "The standardization of inorganic crystal-structure data," *Acta Crystallogr. Sect. A Found. Adv.*, vol. 40, pp. 169–183, 1984.

[60] E. B. Manaia, M. P. Abuçafy, B. G. Chiari-Andréo, B. L. Silva, J. A. Oshiro Junior, and L. A. Chiavacci, "Physicochemical characterization of drug nanocarriers," *Int. J. Nanomedicine*, vol. 12, pp. 4991–5011, 2017.

[61] Z. P. Zahra Pournorouz, Hani Tiznobaik, Joohyun Seo, Amirhossein Mostafavi, Donghyun Shin, "Enhanced specific heat of molten salt nano-eutectic via nanostructural change," *Int. J. Therm. Sci.*, 2018.

[62] M. Salanne and P. A. Madden, "Polarization effects in ionic solids and melts," *Mol. Phys.*, vol. 109, no. 19, pp. 2299–2315, 2011.

[63] B. Chakraborty, J. Wang, and J. Eapen, "Multicomponent diffusion in molten LiCl-KCl:

Dynamical correlations and divergent Maxwell-Stefan diffusivities," *Phys. Rev. E - Stat. Nonlinear, Soft Matter Phys.*, vol. 87, no. 5, pp. 1–7, 2013.

[64] L. Wang, Z. Tan, S. Meng, D. Liang, and G. Li, "Enhancement of molar heat capacity of nanostructured Al2O3," *J. Nanoparticle Res.*, vol. 3, no. 5–6, pp. 483–487, 2001.

[65] m Avramov,I ; Michailov, "Specific heat of," *J. Phys. Condens. Matter*, 2008.

[66] M. R. Saeedian, M.; Mahjour-Shafiei, M.; Shojaee, E.; Mohammadizadeh, "Specific Heat Capacity of TiO2 Nanoparticles," *Comput. Theor. Nanosci.*, vol. 9, no. 4, pp. 616–620, 2012.

[67] W. Luo, W. Hu, and S. Xiao, "Size effect on the thermodynamic properties of silver nanoparticles," *J. Phys. Chem. C*, vol. 112, no. 7, pp. 2359–2369, 2008.

[68] Z. Pournorouz, A. Mostafavi, A. Pinto, A. Bokka, J. Jeon, and D. Shin, "Enhanced thermophysical properties via PAO superstructure," *Nanoscale Res. Lett.*, vol. 12, no. 1, pp. 1–10, 2017.

[69] G. Janz, *Molten salt handbook*. 2013.

[70] N. Araki, M. Matsuura, A. Makino, T. Hirata, and Y. Kato, "Measurement of thermophysical properties of molten salts: Mixtures of alkaline carbonate salts," *Int. J. Thermophys.*, vol. 9, no. 6, pp. 1071–1080, 1988.

[71] A. Grzechnik, P. Bouvier, and L. Farina, "High-pressure structure of Li2CO3," *J. Solid State Chem.*, vol. 173, no. 1, pp. 13–19, 2003.

[72] and E. A. V. Chase Jr., J. L. Curnutt, J. R. Downey Jr., R. A. McDonald, A. N. Syverud, "JANAF Thermochemical Tables, 1982 Supplement," *Phys. Chem. Ref. Data*, vol. 11, no. 3, 2009.

[73] B. S. Hemingway, "Quartz: heat capacities from 340 to 1000 K and revised values for the thermodynamic properties.," *Am. Mineral.*, vol. 72, no. 3–4, pp. 273–279, 1987.

[74] W. L. Burdick,Donald L. ; Leffler, *Petrochemicals in Nontechnical Language*. 2001.

[75] A. Jackson, "Synthetic Versus Mineral Fluids in Lubrication," in *International Tribology*

*Conference*, 1987.

[76] K. C. Ingham, “Precipitation of proteins with polyethylene glycol,” *Methods Enzymol.*, vol. 182, no. C, pp. 301–306, 1990.

[77] G. Paul, M. Chopkar, I. Manna, and P. K. Das, “Techniques for measuring the thermal conductivity of nanofluids: A review,” *Renew. Sustain. Energy Rev.*, vol. 14, no. 7, pp. 1913–1924, 2010.

[78] Z. He and P. Alexandridis, “Nanoparticles in ionic liquids: Interactions and organization,” *Phys. Chem. Chem. Phys.*, vol. 17, no. 28, pp. 18238–18261, 2015.

[79] S. Özerinç, S. Kakaç, and A. G. Yazıcıoğlu, “Enhanced thermal conductivity of nanofluids: a state-of-the-art review,” *Microfluid. Nanofluidics*, vol. 8, no. 2, pp. 145–170, 2010.

[80] cf bonilla, *Nuclear engineering*. 1957.

[81] A. Lenert, *HEAT TRANSFER FLUIDS*. 2012.

## Biographical Information

Zahra Pournorouz received his Bachelor of Science degree in Aerospace engineering from the Amirkabir University of Technology in Tehran in fall 2014. After finishing her bachelor studies, she got admitted directly to Ph.D. program in Mechanical Engineering at the University of Texas at Arlington and joined Dr. Donghyun Shin's nanomaterial research laboratory. Her research was focused on nanofluids and enhance the thermo-physical properties of the conventional nanofluids, which was the first demonstration of the work ever done in this field. She worked on 'investigation of thermo-physical property enhancement mechanism of molten salt nano-eutectic via nanostructural change and polyalphaolefin nanofluid via in situ formation of superstructures" for three years and six months and published several papers. She received his doctoral degree from University of Texas at Arlington in mechanical engineering in summer 2018.